



# Green manufacturing impact on fatigue strength: A comparative analysis of heat-treated AISI 420 and plastically deformed AISI 301LN stainless steels

Maurício Pinheiro dos Santos<sup>a,\*</sup>, Elaine Carballo Siqueira Corrêa<sup>a</sup>,  
Geovane Martins Castro<sup>b</sup>, Waldek Wladimir Bose Filho<sup>c</sup>, Rodrigo Magnabosco<sup>d</sup>,  
Wellington Lopes<sup>a</sup>, Wilian da Silva Labiapari<sup>b</sup>

<sup>a</sup> Department of Materials Engineering, Federal Center for Technological Education of Minas Gerais (CEFET-MG), Belo Horizonte, MG, 30421-169, Brazil

<sup>b</sup> Department of Research and Development, Aperam South America, Timóteo, MG, 35180-018, Brazil

<sup>c</sup> University of São Paulo at São Carlos School of Engineering (USP), São Carlos, SP, 13566-590, Brazil

<sup>d</sup> Department of Materials Engineering, FEI University Center, São Bernardo do Campo, SP, 09850-901, Brazil

## ARTICLE INFO

### Keywords:

Green stainless steel  
Fatigue resistance  
High strength martensitic stainless steel  
Heat treatment  
Transformation induced plasticity (TRIP) steel  
Electron backscattered diffraction (EBSD)

## ABSTRACT

The demand for sustainable and high-performance materials has driven advancements in stainless steel production, including the development of "green stainless steels" that reduce environmental impact without compromising mechanical properties. Traditional steelmaking emits approximately 1.8 tons of CO<sub>2</sub> per ton of steel, whereas the green manufacturing process used in this study replaces coke with sustainably sourced charcoal, significantly lowering emissions while capturing CO<sub>2</sub>.

This study investigates the fatigue behavior of two green high-strength martensitic stainless steels (HSMSS), AISI 420 and AISI 301LN, which differ in composition, microstructure, and processing. AISI 420 underwent quenching and tempering (QT) to achieve a predominantly martensitic structure, while AISI 301LN, a TRIP steel, was cold-rolled with 54 % thickness reduction, inducing partial martensitic transformation. Despite their similar ultimate tensile strength ( $\sigma_{UTS} \sim 1530$  MPa), hardness ( $\sim 46$  HRC), and surface roughness, their fatigue resistance differed significantly.

Through X-ray diffraction (XRD), optical microscopy (OM), scanning electron microscopy (SEM), and Electron Backscatter Diffraction (EBSD), this study explores how distinct processing routes influence microstructural evolution and fatigue performance. The results provide insights into how sustainable manufacturing methods contribute to fatigue resistance while addressing environmental concerns.

## 1. Introduction

Stainless steel (SS) is a versatile material widely used across various industries due to its durability, corrosion resistance, and aesthetic appeal, with increasing applications in structural uses in recent years. However, SS is not a single-phase material; it can exhibit a variety of microstructures, such as austenite ( $\gamma$ ), ferrite ( $\alpha$ ), and martensite ( $\alpha'$ ). With an appropriate combination of alloying elements, SS can be fully austenitic, a mixture of  $\alpha$  and  $\gamma$ , fully ferritic, or martensitic. Its use for structural applications, particularly in mildly corrosive environments, has steadily grown in industries like aerospace, nuclear energy, petrochemicals, and automotive. These industries rely on SS's excellent corrosion resistance and moderate to high deformability. Given the cyclic loading conditions in these sectors, fatigue properties play a critical

role in determining the material's performance and reliability under service conditions. As SS competes with carbon steels and aluminum in these sectors, comprehensive fatigue data is crucial for evaluating its service life under such conditions [1–4].

Currently, martensitic stainless steels (MSS) are particularly valued for their excellent corrosion resistance combined with medium to high mechanical strength and toughness. These properties make MSS ideal for structural applications requiring both durability and mechanical performance. The strength and hardness of MSS can further be enhanced through heat treatments (HT), which involve quenching and tempering. During quenching,  $\gamma$  transforms into  $\alpha'$  as the material is rapidly cooled from high temperatures, stabilizing the martensitic phase. This HT-induced transformation is primarily governed by the material's chemical composition, with high chromium content providing significant

\* Corresponding author.

E-mail address: [arauceas@gmail.com](mailto:arauceas@gmail.com) (M. Pinheiro dos Santos).

<https://doi.org/10.1016/j.jmrt.2025.03.087>

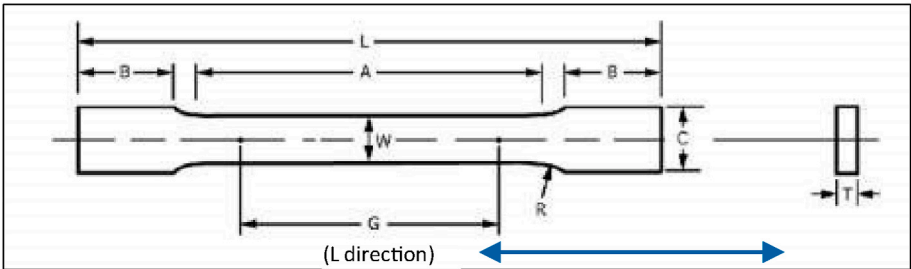
Received 18 October 2024; Received in revised form 5 March 2025; Accepted 10 March 2025

Available online 11 March 2025

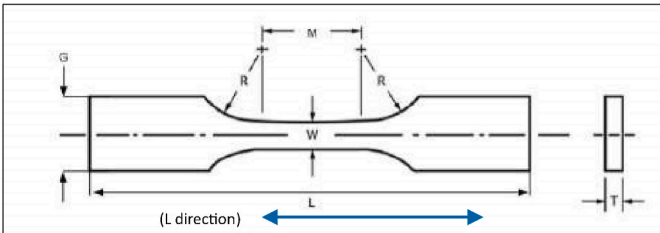
2238-7854/© 2025 The Authors. Published by Elsevier B.V. This is an open access article under the CC BY-NC license (<http://creativecommons.org/licenses/by-nc/4.0/>).

**Table 1**  
Chemical composition of HSMSS (wt. - %).

| Material   | C     | Mn   | Cr    | Si   | Ni   | Mo   | N    | Fe      |
|------------|-------|------|-------|------|------|------|------|---------|
| AISI 301LN | 0.023 | 1.50 | 17.31 | 0.44 | 6.77 | 0.04 | 0.11 | Balance |
| AISI 420   | 0.200 | 0.18 | 12.03 | 0.39 | 0.20 | 0.02 | 0.01 | Balance |



**Fig. 1.** Schematic representation of the static tensile specimens ( $t = 2.75$  mm,  $L = 213$  mm,  $G = 75$  mm,  $A = 93$  mm,  $B = 60$  mm,  $C = 20$  mm,  $R = 13$  mm, and  $W = 12.5$  mm).



**Fig. 2.** Schematic representation of the fatigue specimens ( $t = 2.75$  mm,  $L = 153$  mm,  $G = 20$  mm,  $M = 18$  mm,  $R = 72$  mm, and  $W = 9$  mm).

**Table 2**  
Stress levels for fatigue tests with a stress-ratio ( $\sigma_{min}/\sigma_{max}$ )  $R = 0.1$ .

| R   | Level 1                | Level 2                | Level 3                | Level 4                | Level 5                |
|-----|------------------------|------------------------|------------------------|------------------------|------------------------|
| 0.1 | $0,95 \times \sigma_y$ | $0,90 \times \sigma_y$ | $0,85 \times \sigma_y$ | $0,80 \times \sigma_y$ | $0,75 \times \sigma_y$ |

**Table 3**  
Deformation levels applied in AISI 301LN SS.

| AISI 301LN       | Final thickness (mm) | Reduction (mm)  | True strain, $\epsilon$ | Hardness (HRC) |
|------------------|----------------------|-----------------|-------------------------|----------------|
| As-received      | 6.00                 | 0               | 0                       | –              |
| 20 % cold rolled | $4.81 \pm 0.05$      | $1.19 \pm 0.05$ | 0.20                    | $35 \pm 1$     |
| 28 % cold rolled | $4.32 \pm 0.05$      | $0.49 \pm 0.05$ | 0.40                    | $43 \pm 0.5$   |
| 39 % cold rolled | $3.66 \pm 0.05$      | $0.66 \pm 0.05$ | 0.60                    | $45 \pm 0.6$   |
| 54 % cold rolled | $2.76 \pm 0.05$      | $0.90 \pm 0.05$ | 0.85                    | $47 \pm 0.3$   |
| 59 % cold rolled | $2.41 \pm 0.05$      | $0.35 \pm 0.05$ | 1.15                    | $50 \pm 0.6$   |

hardenability and tempering reducing the risk of cracking in complex geometries [5,6].

In contrast, in austenitic stainless steels (ASS), martensitic transformation can also occur through plastic deformation rather than HT. This process, known as deformation-induced martensitic transformation, occurs under mechanical strain at lower temperatures and is characteristic of transformation-induced plasticity (TRIP) steels. During deformation, the crystal structure of  $\gamma$  changes to  $\alpha'$ , increasing the material's strength and toughness, making TRIP steels an attractive

option for demanding fatigue applications [7,8].

The comparison of both materials is crucial in industrial final use applications due to their potential for improved functionality and reliability. Each manufacturing method has its advantages and disadvantages, highlighting the importance of selecting appropriate processing techniques for specific material properties. In response to global competition, industries now require higher levels of safety, durability, and reliability. As a result, lightweight vehicles, and structures that are both safe and economically sustainable demands the efficient use of superior materials proprieties, particularly in the context of green stainless steel development, while ensuring the prevention of premature structural failures. This emphasis on sustainable manufacturing processes, combined with the need for reliable structural performance, highlights the importance of understanding material fatigue behavior under service conditions [9–11].

Therefore, new green materials also must be designed and tested for sufficient resistance to mechanical stress for applications in a wide variety of products on the market, so that the dispersions of this resistance to the applied load in the material must be quantified for any subsequent reliability analysis [2,12,13]. While the effects of cold work and heat treatments on the tensile properties and toughness of MSS have been extensively studied, the fatigue performance of these materials in structural applications has received less attention. Fatigue strength is a crucial parameter for structural components, especially when these materials are considered as alternatives to traditional structural steel. The fatigue limit is particularly important engineers, as it defines the material's endurance under cyclic loads. This study seeks to address the gap in literature by providing insights into the fatigue behavior of green MSS in possible use for structural applications.

Based on this context, the present work investigated the fatigue resistance of AISI 301LN and AISI 420 green stainless steels, selected for their chemical compositions, microstructural characteristics, and processing methods, which reflect two distinct approaches to achieving a martensitic microstructure [14]. AISI 420 and AISI 301LN differ significantly in terms of their production costs, with AISI 420 typically priced at approximately \$3.50–\$4.00 per kilogram and AISI 301LN at \$4.50–\$6.00 per kilogram, depending on market conditions and processing specification [15,16]. Although these prices are higher than carbon steel, which averages around \$1.00–\$1.50 per kilogram, their superior corrosion resistance and durability can justify the cost for critical structural components. Thus, it has been determined the fatigue limit of both steels by constructing S–N curves and characterizing their microstructure before and after heat treatments and plastic deformation. Finally, it was compared the fatigue resistance of heat-treated and



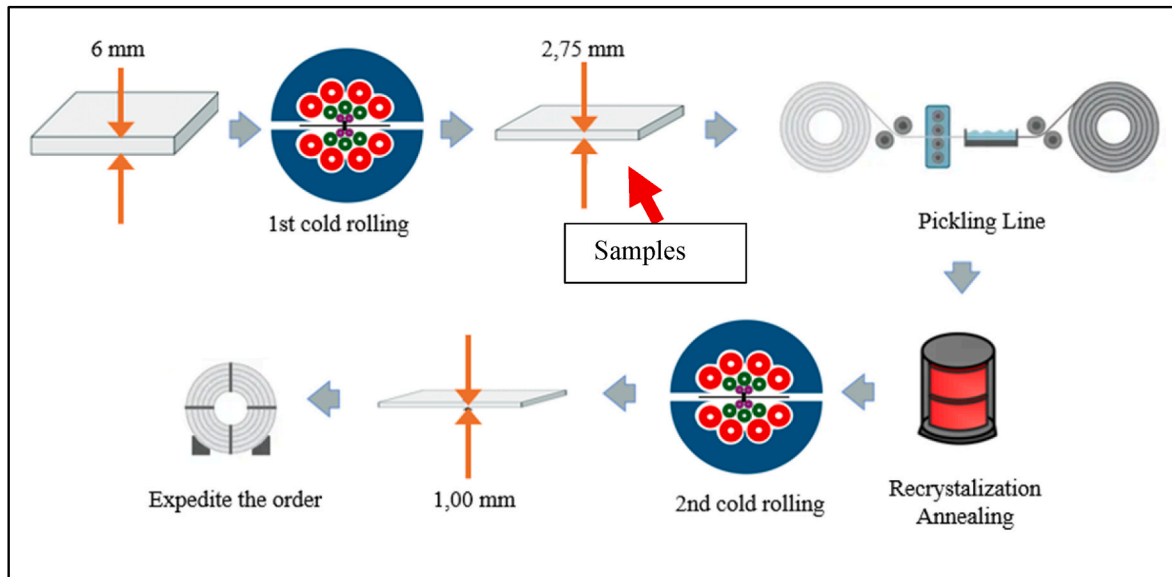


Fig. 3. Schematic representation of the cold rolling process and where the samples were collected.

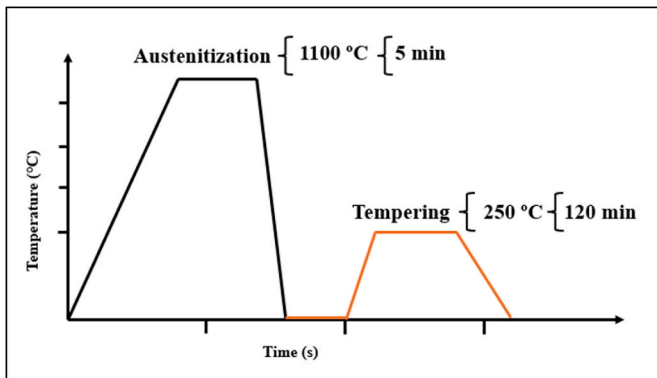


Fig. 4. Schematic representation of the quenching and tempering process as suggested by A.N. Moura et al. [23].

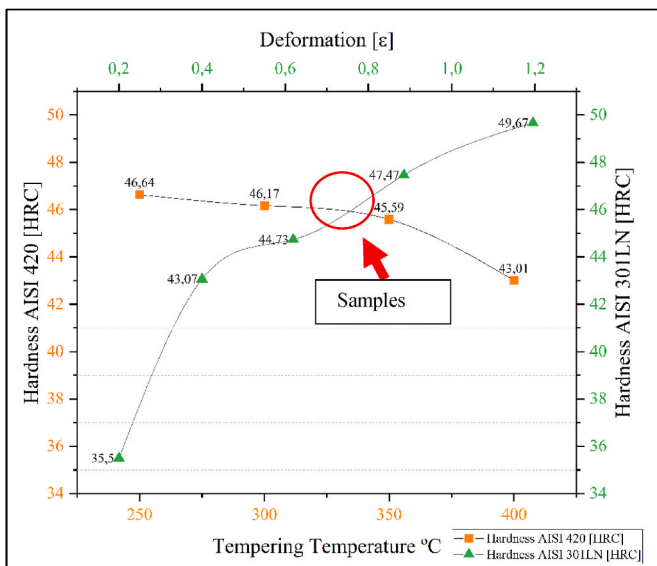


Fig. 5. Work hardening curve of AISI 301LN SS vs. Heat treatment (quenching at 1100 °C) curve of AISI 420 SS.

plastically deformed steels, observing the influence of different manufacturing processes on the material's ability to withstand cyclic loads.

## 2. Experimental procedure

### 2.1. Materials

The materials used in this research were AISI 420 and AISI 301LN SS supplied by Aperam South America, internally denominated as ACE P420D and ACE P301L SS and rolled in coil form. The AISI 420 SS, which initially had a nominal thickness of 6 mm with a tolerance of  $\pm 0.05$  mm, was hot rolled to reach a final thickness of 2.75 mm. Finally, it underwent a quenching and tempering heat treatment. The AISI 301LN SS used in this study, which initially had a nominal thickness of 6 mm with a tolerance of  $\pm 0.02$  mm, underwent cold rolling using an industrial Sendzimir-type mill, progressively reducing its thickness to achieve the desired levels of deformation. The final thicknesses for the cold-rolled samples were 4.81 mm (20 % reduction), 4.32 mm (28 % reduction), 3.66 mm (39 % reduction), 2.76 mm (54 % reduction), and 2.41 mm (59 % reduction), as indicated in Table 3. Each reduction stage was measured with a precision of  $\pm 0.05$  mm. The material's average chemical compositions were obtained using three techniques. The nitrogen content was measured through thermal conductivity difference (Leco ON736) and the carbon through Nondispersive Infrared Absorption (Leco CS844). The other elements content was determined through X-ray fluorescence spectrometry (ARL9900), detailed in Table 1.

### 2.2. Metallography – microstructure

The microstructural characteristics in as-received and after-processed conditions were assessed using OM and EBSD. The procedure for preparing the samples for metallographic analysis was carried out through the following steps: cutting, embedding, grinding, polishing, and chemical etching. The specimen was cut in the central region of the thickness and the longitudinal direction of each sample condition performed, using abrasive cutting discs [17]. For hot embedding, a Bakelite-type resin was used. Subsequently, grinding from #120 up to #1200 grit sandpaper on a Struers Abramin-A grinder for approximately 150s for each sandpaper. After this step, the sample was polished with a diamond polishing agent (DP-Spray P) in sizes of 9, 3, and 1  $\mu$ m on a Struers Abramin-B polisher, for approximately 420s for each abrasive.

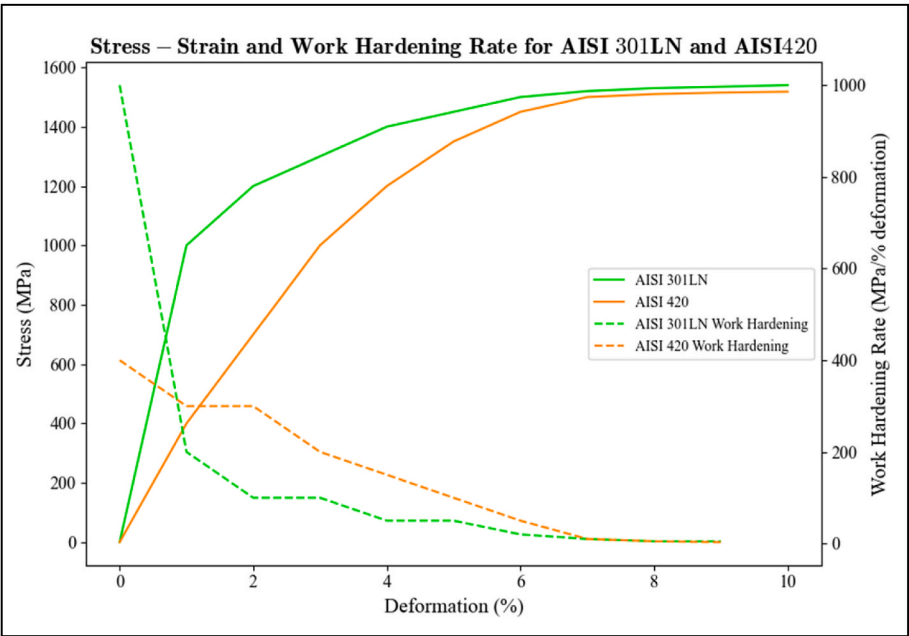


Fig. 6a. The stress–strain curves and corresponding work hardening rate curves for AISI 301LN and AISI 420.

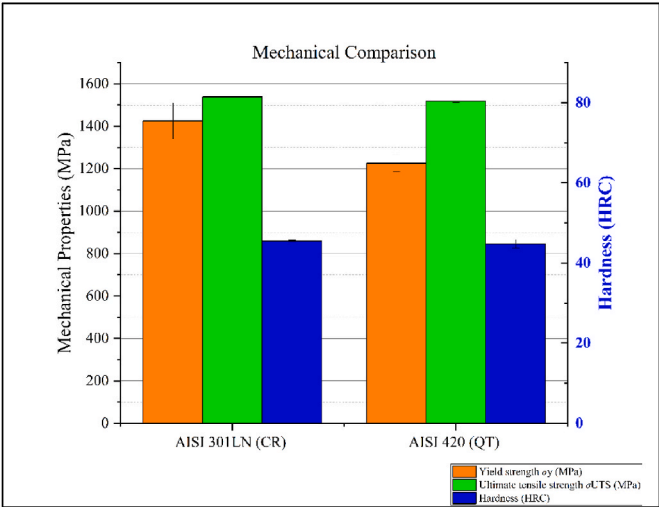


Fig. 6b. Mechanical properties of tested SS, and standard uncertainty (u) associated.

The metallographic specimens of the AISI 420 samples were etched with Vilella reagent (95 ml of ethyl alcohol, 1 g of picric acid, and 3 ml of HCl), with an immersion time of 50s. The AISI 301LN samples were etched with a 10 % oxalic acid solution, 6 V for 90 s at room temperature. Finally, the samples were washed with water, and alcohol, and dried with hot air [18].

Table 4  
Surface roughness parameter data for as-polished samples.

| AISI 301LN  |         |         | AISI 420    |         |         |
|-------------|---------|---------|-------------|---------|---------|
| As polished | Ra (μm) | Rt (μm) | As polished | Ra (μm) | Rt (μm) |
| #01–95 %    | 0.08    | 0.81    | #02–95 %    | 0.08    | 0.72    |
| #08–90 %    | 0.09    | 0.70    | #06–85 %    | 0.15    | 1.70    |
| #14–85 %    | 0.19    | 2.41    | #10–75 %    | 0.07    | 0.87    |
| #19–80 %    | 0.04    | 0.57    | #14–65 %    | 0.10    | 1.17    |
| #26–75 %    | 0.13    | 1.48    | #17–60 %    | 0.19    | 1.76    |
| #31–70 %    | 0.11    | 1.10    | #19–55 %    | 0.13    | 1.67    |
| #49–68 %    | 0.13    | 1.57    | #23–45 %    | 0.15    | 1.65    |
| #40–65 %    | 0.07    | 0.72    | #24–40 %    | 0.09    | 1.47    |
| Average     | 0.83    | 1.17    | Average     | 0.12    | 1.38    |
| σ2          | 0.002   | 0.34    | σ2          | 0.002   | 0.14    |

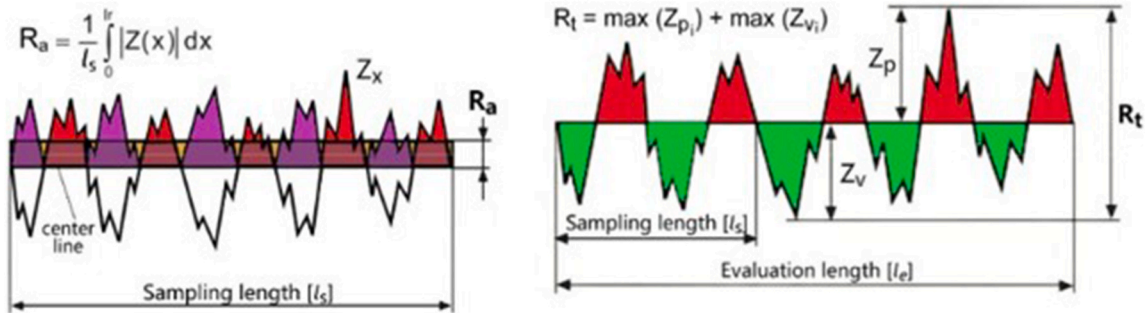
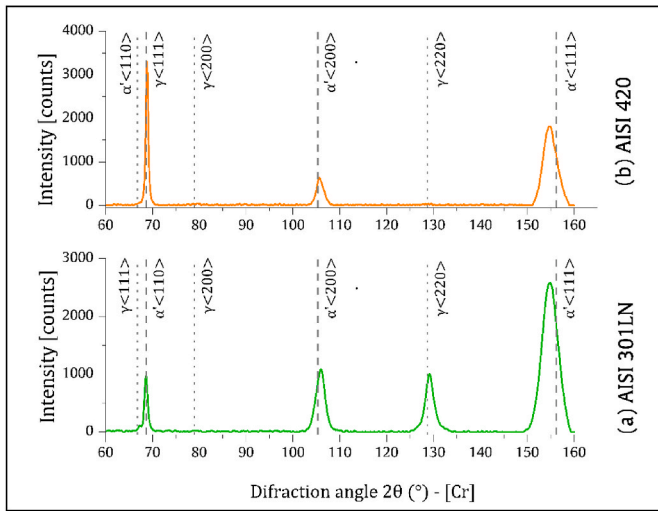


Fig. 7. Schemes for various parameters estimating the state of the samples surface after polishing: Ra: arithmetical mean deviation; Z(x): absolute ordinate value; Rt: total height of profile; Zp: largest profile peak height; Zv: largest profile valley depth.



**Fig. 8.** (a) cold-worked material with 54 % plastic deformation; (b) Heat treated material (quenched 1100 °C and tempered 250 °C).

### 2.3. SEM-FEG-EBSD - fractography analysis

A SEM-FEG, model Quanta 250 from the Aperam South America Research Center with an EBSD - Electron Backscatter Diffraction acquisition device, was used. The scanning area was  $600 \times 600 \mu\text{m}$ , with an increment of  $1 \mu\text{m}$  between passes. The result analysis and image composition were performed using the OIM Analysis TM-TSL-EDAX software. The points in the maps with a confidence index (CI) below 0.095 were disregarded in the data analysis. Scanning electron microscopy (SEM) was conducted to investigate the influence of internal

defects, such as inclusions, on fatigue performance. SEM images were acquired using a Philips XL30 – LaB6 with a magnification of 20x to 500000x. Samples of both materials were examined after processing to capture the most extreme results.

### 2.4. Mechanical testing

To evaluate the mechanical properties, both uniaxial tensile and hardness tests were conducted. Static tensile tests were carried out using an INSTRON 5583 servo hydraulic machine with 150 kN load capacity. Standard-sized tension test specimens were machined to the dimensions shown in Fig. 1. The mechanical properties were determined in accordance with ASTM E8/E8M – 11 [19] at a constant crosshead velocity of 0.5 mm/min. The specimens were tested in the longitudinal (L) direction using an optical strain measurement feature measuring deformation throughout the entire test until sample failure. The hardness tests were carried out using an Instron Wolpert 930 tester according to ASTM E92-17 [20]. Five measurements were carried out on each sample.

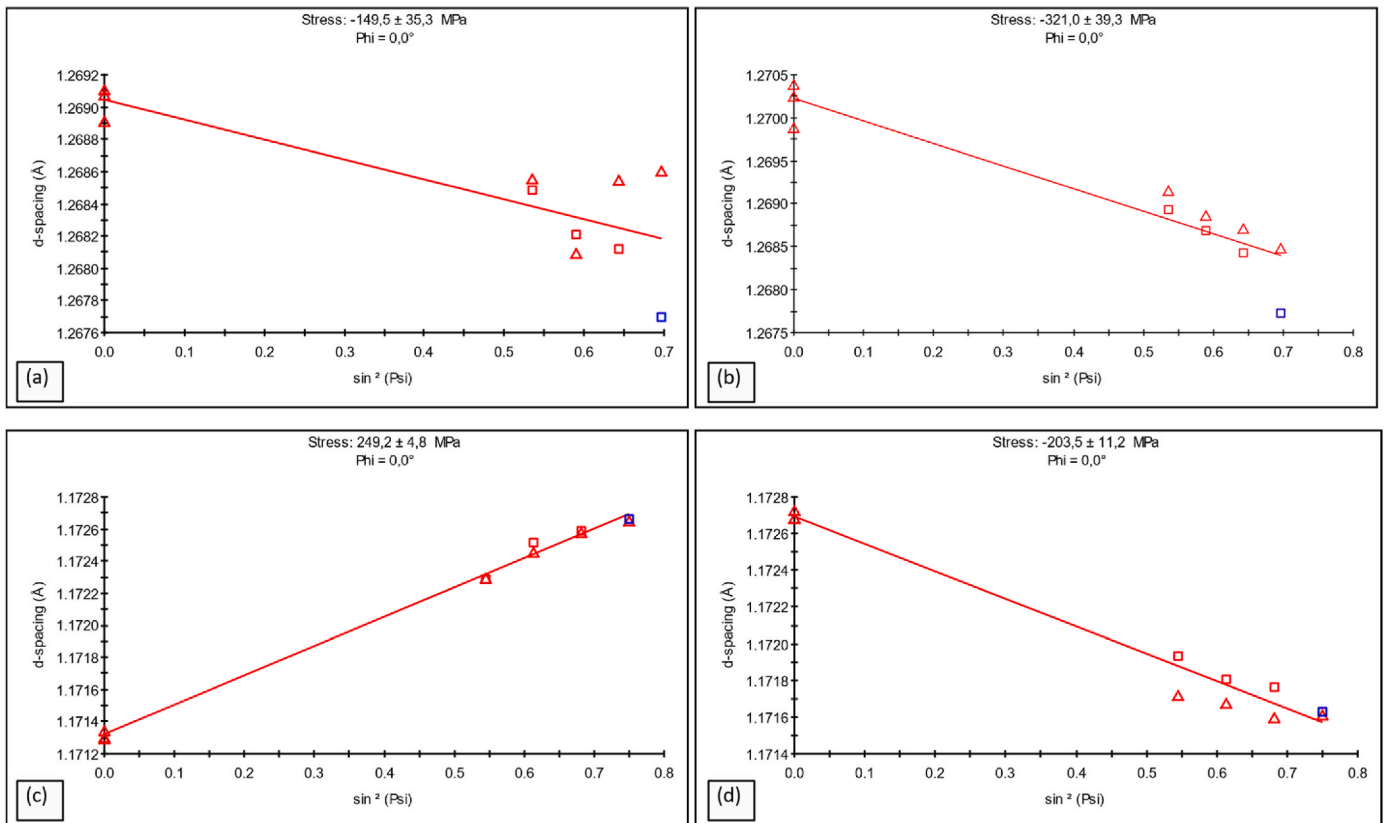
### 2.5. Fatigue test

Constant amplitude high-cycle fatigue (HCF) tests were conducted at room temperature,  $\cong 23^\circ\text{C}$ , using an Instron servo hydraulic test frame. An R-ratio of 0.1 ( $\sigma_{\text{min}}/\sigma_{\text{max}}$ ) and a frequency of 21 Hz were

**Table 5**

Volume fractions (absolute) (%) of the found  $\alpha'$  - martensite in the as-deformed and heat-treated samples determined by EBSD and ferritoscope.

| Samples                                     | EBSD             | FERRITOSCOPE     |
|---|------------------|------------------|
| AISI 301LN steel (54 % plastic deformation) | $39.3 \pm 1.05$  | $41.3 \pm 0.7$   |
| AISI 420 steel (heat treated)               | $97.95 \pm 0.25$ | $86.97 \pm 3.84$ |



**Fig. 9.** (a) AISI 301 LN CR material with 54 % plastic deformation (Surface residual Stress:  $149.5 \pm 35.3 \text{ MPa}$ ), (b) thickness in the longitudinal (Residual Stress:  $321 \pm 39.3 \text{ MPa}$ ); (c) AISI 420 QT material (Surface residual Stress:  $249.2 \pm 4.8 \text{ MPa}$ ), (d) thickness in the longitudinal (Residual Stress:  $203.5 \pm 11.2 \text{ MPa}$ ).



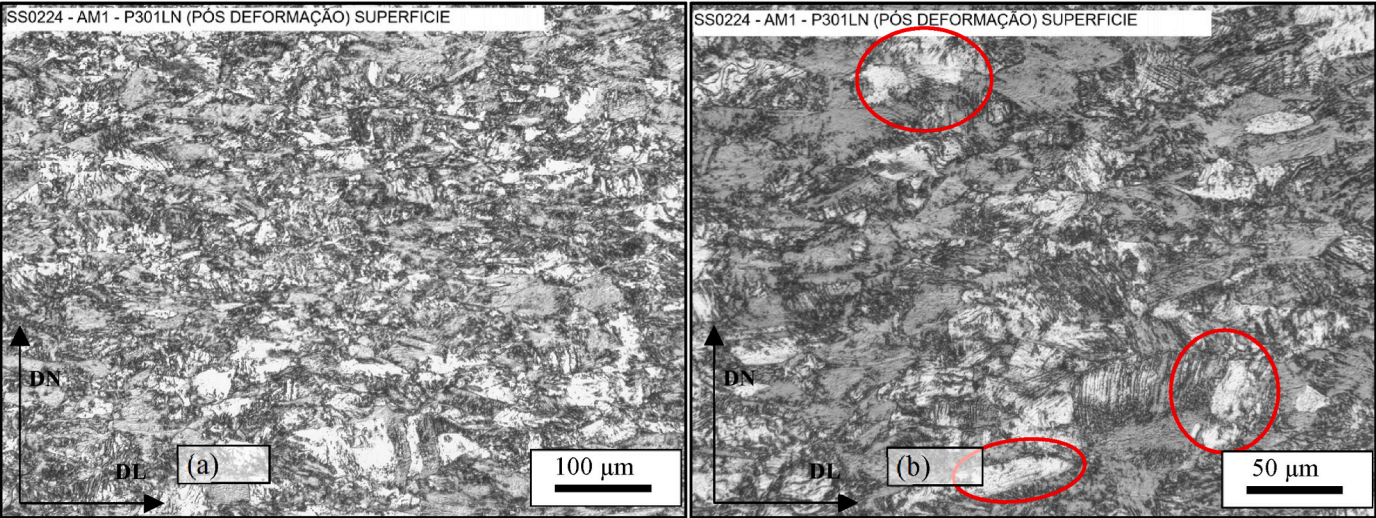


Figure 10. (a), (b). Surface optical microscopy of the AISI 301LN SS after it has been deformed 54% in cold work.

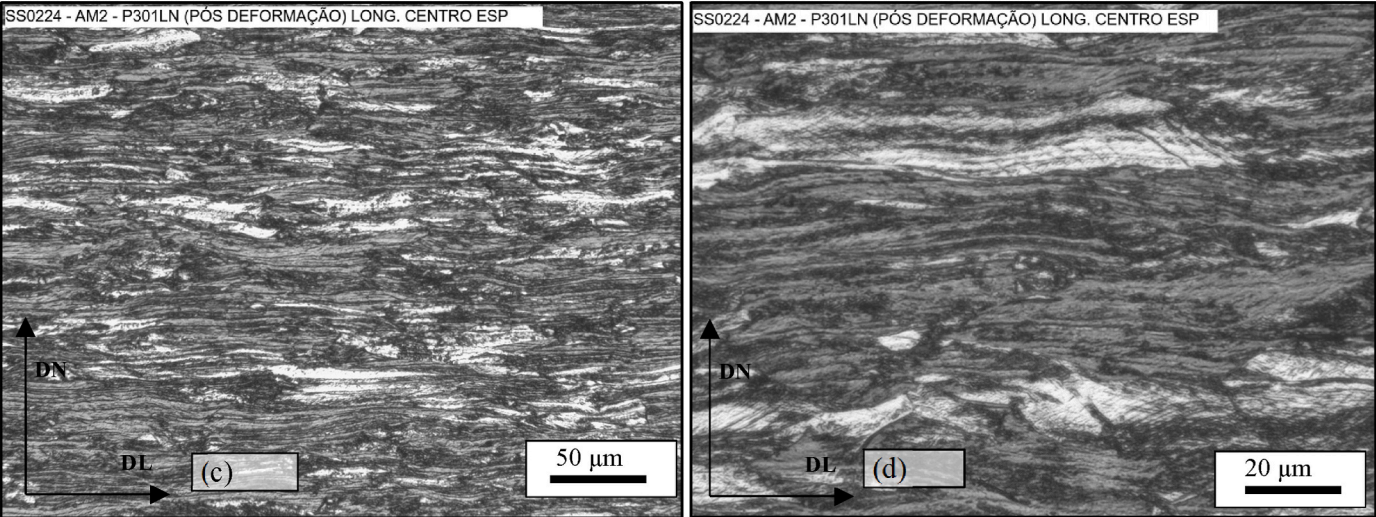


Fig. 10. Fig. 10(a), (b). Surface optical microscopy of the AISI 301LN SS after it has been deformed 54 % in cold work. Fig. 10(c) 10(d) longitudinal AISI 301LN SS etched with 10 % Behara reagent. 10(c) and (d) are the same sample but with higher magnification.

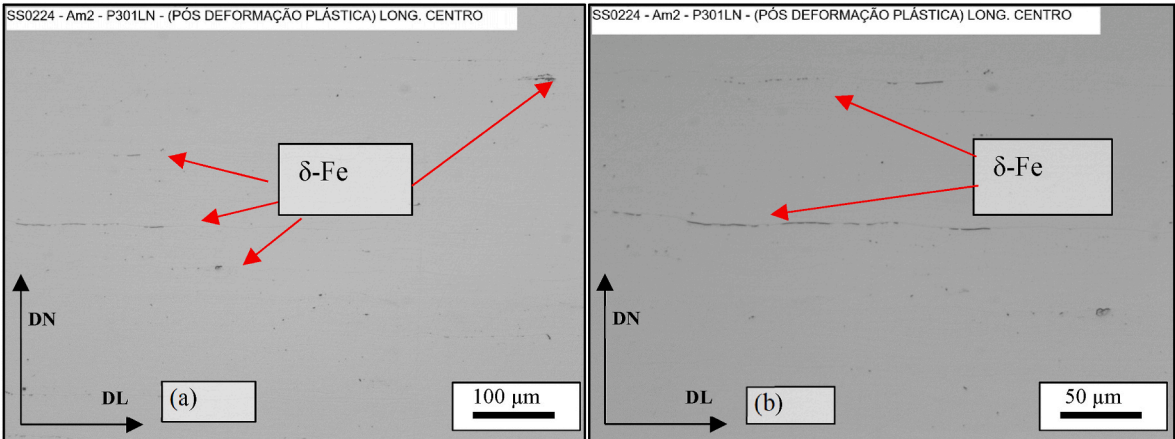
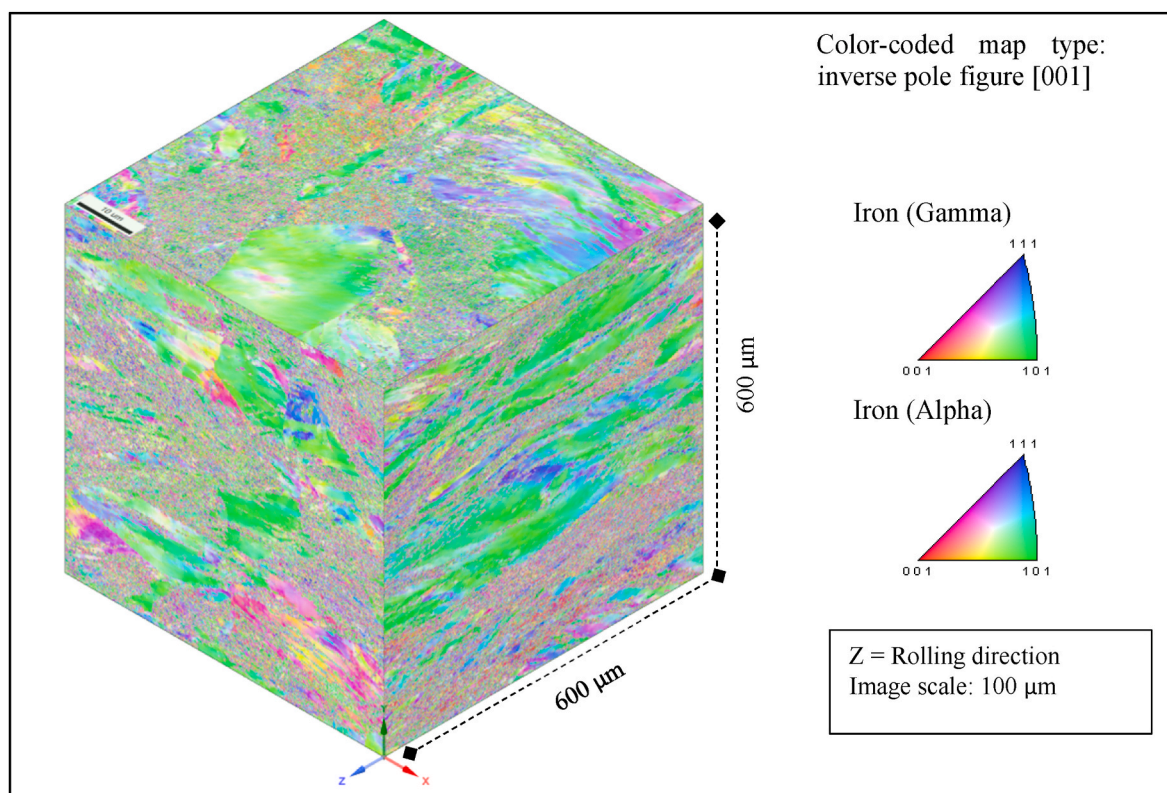


Fig. 11. Microstructure of AISI 301LN SS samples in the longitudinal direction after plastic deformation (electropolishing and etching with 10 % NaOH).





**Fig. 12.** Inverse Pole Figure (IPF) maps showing the normal direction (y), rolling direction (z), and transverse direction (x) generated for the 54 % cold worked AISI 301LN SS samples.

maintained throughout the tests. A range of maximum applied stress values was used to generate a stress ( $\sigma_{max}$ ) – number of fatigue cycles to failure (Nf) curve. The total fatigue life, Nf, was determined by considering the complete fracture of the specimen as the failure criterion, except for tests that exceeded 106 cycles, which were considered "run out." Only coupons with cracks originating at the neck of each specimen were considered valid.

Standard-sized fatigue test specimens were machined prepared by a Fanuc Wire Electrical Discharge Machining (EDM), requiring a maximum edge roughness average (Ra) of 0.5  $\mu\text{m}$  according to ASTM E466 [21,22], with a geometry shown in Fig. 2. Initially, five distinct stress amplitude levels were established for the tests, as detailed in Table 2. The highest level reached a maximum stress of  $0.95 \times \sigma_y$  and the minimum  $0.75 \times \sigma_y$  initially. This range was selected to generate a series of data points on the S–N curve, spanning from 103 to 106 cycles. To ensure the integrity of the thin material ( $\cong 2.8 \text{ mm}$ ), fatigue testing was carried out at a frequency of 21 Hz with a load ratio (R) of 0.1, thereby avoiding compressive stresses. All the samples were analyzed in as-polished condition indicating that the sample surface was prepared through standard metallographic polishing techniques to remove surface irregularities and achieve a uniform finish.

## 2.6. Cold rolling

For the cold rolling process of AISI 301LN SS, an industrial Sendzimir-type rolling mill, internally at Aperam referred to as LB3, was used. This equipment performs cold rolling of extremely hard materials and very thin thicknesses, allowing the development of new products, as well as improvements and optimization in the production process. Although the material was cold rolled up to 59 % reduction, the 54 % cold rolled condition was selected for further study as it achieved a hardness level comparable to that of the quenched and tempered AISI 420 material. To maintain the similarity in mechanical properties

between the cold-rolled samples and the heat-treated material, no annealing heat treatment was conducted following the cold-rolling processes, thus, the material was analyzed as-deformed as shown in schematic of Fig. 3.

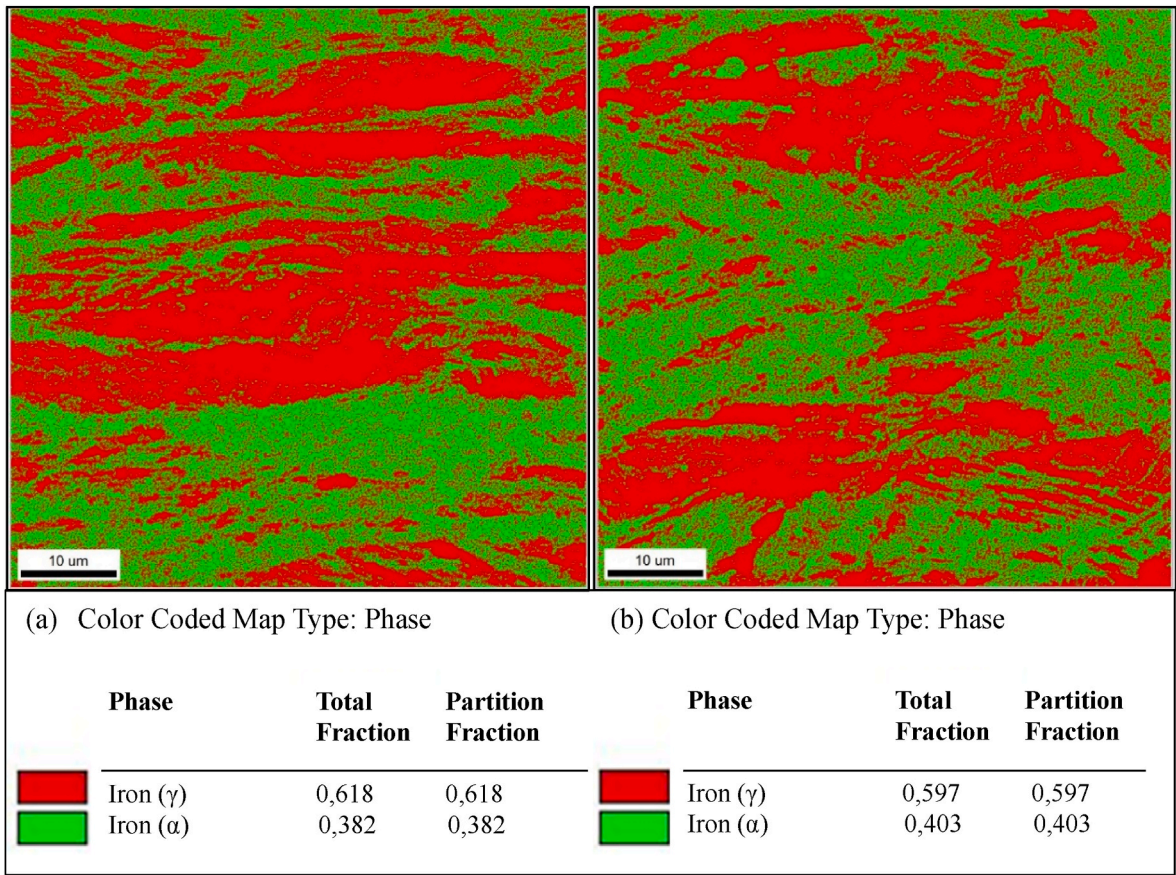
## 2.7. Quenching and tempering heat treatment

For the austenitization and quenching process, a resistive furnace with a refractory chamber and an inert nitrogen gas atmosphere was used. The maximum operating temperature reaches 1400 °C. To ensure temperature uniformity, all samples were positioned in the central region of the furnace with a metallic base made of AISI 310 SS. The target temperature of austenitization was 1100 °C, according to a study conducted by A.N. Moura et al. [23], in which complete martensitic transformation was observed in AISI 420 SS after this treatment. After a soaking period of 5 min at 1100 °C, the quenching process was carried out with forced air cooling, using a blower with a lower and upper cyclone-type blowing system to guarantee homogeneous cooling of the samples. Subsequently, the samples were tempered at 250 °C for 120 min to achieve the desired microstructural condition, as shown in the schematic of Fig. 4.

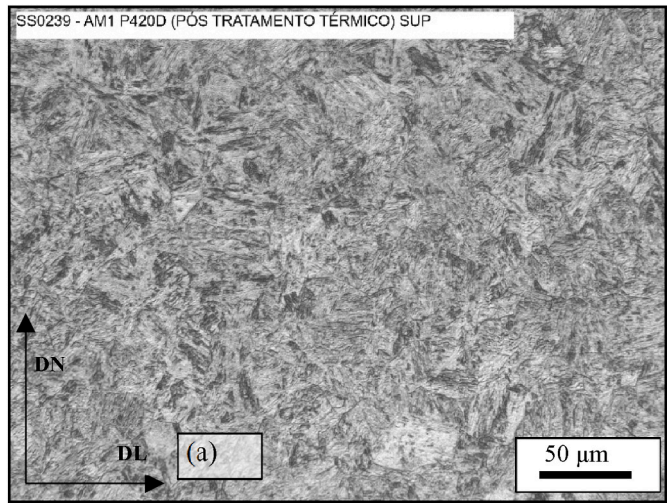
## 2.8. Hardness test

As described in ISO 6508-1 [24], HRC microhardness measurements were carried out along the entire useful region of specimens, in both conditions, as received, heat treated and plastically deformed. Measurements were taken at longitudinal sections of the specimens, at 6 points, with a spacing of approximately 0.5 mm each. The microhardness measurements were performed with an Instron Wolpert, model Testor 930 micro-durometer, using 5 kgf load.





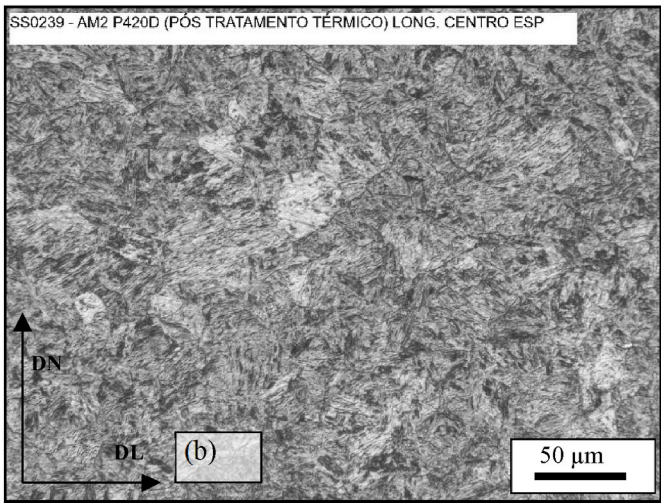
**Fig. 13.** (a) longitudinal direction, Fig. 13(b) transverse direction, Phase map of the AISI 301LN SS sample observed using the EBSD technique. Red phase (austenite), green phase ( $\alpha'$  martensite).



**Fig. 14.** Surface microstructure of AISI 420 SS after quenching and tempering heat treatment (Vilella etch).

2.9. Residual stress and crystal structure

The specimen’s longitudinal direction residual stress analysis (side thickness of material) was performed using the X-ray diffractometer Shimadzu XRD7000 (Cr Tube). The same experimental arrangement was used to identify phases by X-ray diffraction, and these measurements have been confirmed with the Helmut Fischer MP30 ferritoscope. Due to

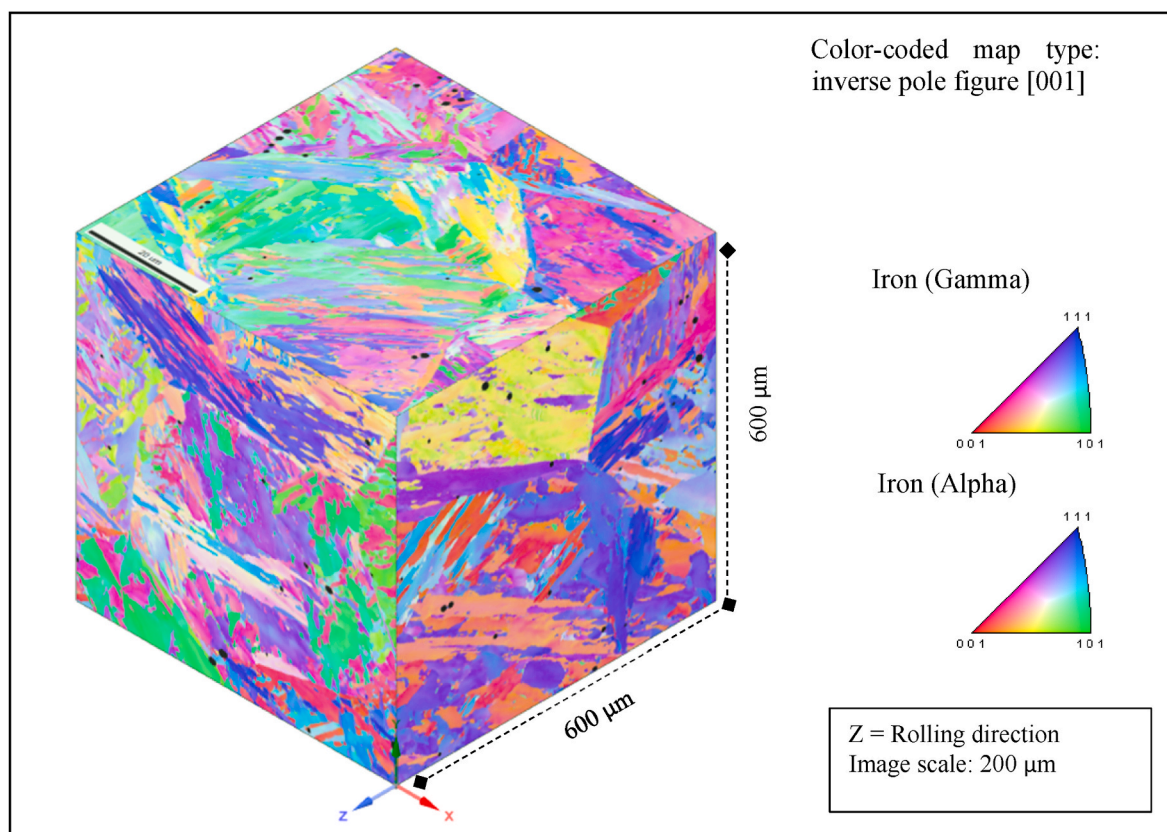


**Fig. 15.** Microstructure of AISI 420 SS, longitudinal thickness, after quenching and tempering, etched with Vilella solution.

the geometry of the specimens, particularly their thickness, 2.75 mm, measuring the residual stress in the critical area required a specialized setup involving the mounting of multiple specimens.

3. Experimental results

To establish a correlation between hardness and thickness of the



**Fig. 16.** Inverse Pole Figure (IPF) maps showing the normal direction (y), rolling direction (z), and transverse direction (x) generated for the quenched and tempered AISI 420 SS samples.

materials, heat treatments of quenching and tempering were conducted on AISI 420 SS and plastic deformation on AISI 301LN SS. The AISI 420 SS as-received condition was obtained hot rolled (ferritic microstructure) at the final thickness reduction from the industrial rolling mill. Then, the samples were prepared and austenitized at 1100 °C for 15 min in a muffle furnace and forced air-quenched. The samples were tempered at 250 °C for 120 min. For the AISI 301LN SS, the as-received condition underwent an industrial plastic deformation of 0.20, 0.28, 0.39, 0.54, and 0.59 and was analyzed as-deformed, Table 3.

Hardness values and the associated rolling pass plan for samples taken from a 2.75 mm sheet after 54 % cold rolling in an industrial line are presented in Table 3. This data provides insights into the relationship between cold rolling parameters and the resulting mechanical properties of the material. The graph with the results reveals the presence of two curves that intersect at approximately  $46 \pm 1$  HRC with a thickness of  $2.75 \text{ mm} \pm 0.02 \text{ mm}$ . The results are graphically represented in Fig. 5.

Fig. 6(a) presents the stress–strain curves and corresponding work hardening rate curves for AISI 301LN and AISI 420 HSMSS, while Fig. 6 (b) presents the average mechanical property values and their associated standard uncertainties (u) for the tested steels. Mechanical properties were determined following the ASTM E8/E8M – 11 standard at a constant crosshead speed of 7 mm/min. Longitudinal (L) direction testing was conducted using an optical strain measurement feature to monitor deformation until specimen failure [19]. The AISI 420 steel curve exhibits a higher initial yield stress but a more modest work hardening rate, reflecting its stable microstructure and limited capacity for plastic deformation, consistent with findings for quenched and tempered martensitic steels [25]. In contrast, the AISI 301LN (metastable austenitic) curve starts at a slightly lower yield stress but demonstrates a significantly higher and more sustained work hardening rate. This pronounced strain-hardening behavior is attributed to the TRIP (Transformation-Induced Plasticity) effect, where deformation induces the

partial transformation of austenite into martensite, thereby enhancing strength and delaying necking [26]. The direct comparison of the stress–strain responses and work hardening evolution in Fig. 6(a) highlights the critical role of the mixed microstructural evolution in the deformation behavior of AISI 301LN—a factor that becomes particularly significant when evaluating fatigue performance in later sections of this study.

### 3.1. Surface roughness

Previous literature has found that surface roughness parameters exhibit a strong influence on the fatigue behavior of metals.

[27,28]. It has been reported that surface parameters such as Ra and Rt have the strongest correlation to early crack nucleation on HCF life in metals [27,29]. Therefore, within this work, attention has been paid to the Ra and Rt surface parameters, where the Ra value gives a representation of the arithmetic mean deviation within a roughness profile, while the Rt value represents the total profile height as showed in Fig. 7, [28–30]. The surface roughness parameters recorded from the profilometer are displayed in Table 4 [22].

From Tables 4, it can be observed that among the as-polished AISI 301LN SS samples, sample #14 exhibited the highest surface roughness (Rt) value at 2.41  $\mu\text{m}$ , while sample #19 displayed the lowest Rt value of 0.57  $\mu\text{m}$ . The overall average Rt value for the polished specimens was 1.17  $\mu\text{m}$ . Within the group of AISI 420 SS polished samples, the highest and lowest Rt values were observed in samples #17 and #02, respectively, with values of 1.76  $\mu\text{m}$  and 0.72  $\mu\text{m}$ . Notably, there was less variation in surface roughness among the AISI 420 SS samples compared to the AISI 301LN SS samples, as indicated by the lower variance ( $\sigma_2 = 0.14$  for AISI 420 and  $\sigma_2 = 0.34$  for AISI 301LN).

The EDM cutting and polishing process is expected to have significantly reduced the variation in height profiles, resulting in a very low



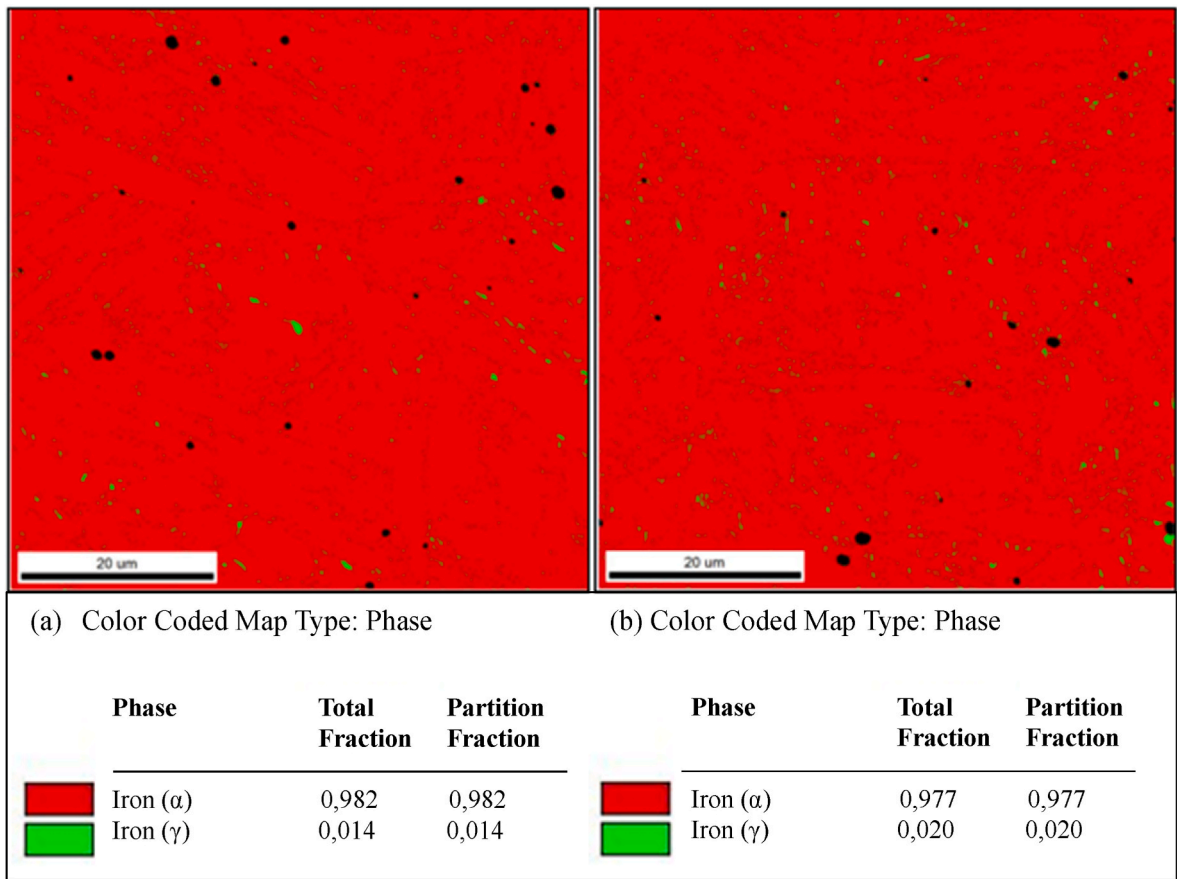


Fig. 17. (a) longitudinal direction, Fig. 17 (b) transverse direction, Phase map of the AISI 420 SS sample observed using the EBSD technique. Martensite (red), retained austenite (green), and (Cr,Fe)23C6 carbides (black).

overall Rt and Ra value for both materials. This smoother surface and reduced variation should theoretically enable the samples to withstand a greater number of fatigue cycles and higher maximum applied stresses ( $\sigma_{max}$ ) by minimizing stress concentration features that can initiate fatigue failure prematurely [27,31]. Therefore, it is hypothesized that the polished samples will exhibit a longer fatigue life than the as-received samples, although the latter were not subjected to fatigue analysis in this study [32]. Given the similar surface finish and low variation in Rt and Ra between the materials, a direct comparison of fatigue life is anticipated.

3.2. X-ray diffraction

Fig. 8 (b) presents the XRD patterns of the AISI 301 LN HSMSS samples subjected to cold rolling in the industrial line. As the cold rolling reduction increases to 54 %, the intensity of the austenite ( $\gamma$ ) peaks diminishes, indicating a progressive transformation to  $\alpha'$  - martensite [23, 33]. However, beyond this deformation level, martensite content plateaus rather than increasing linearly. This suppression is linked to adiabatic heating during high-strain-rate plastic deformation, as observed by Talonen and Nenonen (2005) [34]. At elevated strain rates (e.g.,  $200\text{ s}^{-1}$ ), the energy dissipated as heat raises the material's temperature, stabilizing the austenite phase and reducing the thermodynamic driving force for  $\gamma \rightarrow \alpha'$  transformation. Consequently, despite continued deformation, thermal stabilization counteracts further martensite nucleation, leading to saturation beyond a critical strain threshold [34].

The XRD patterns, acquired using Cr  $K\alpha$  radiation, reveal distinct intensity peaks corresponding to different crystallographic planes within the  $2\theta$  range of  $60^{\circ}$ – $165^{\circ}$ . Analysis of these patterns confirms the

coexistence of both austenite ( $\gamma$ ) and martensite ( $\alpha'$ ) phases [35].

The most prominent peaks are attributed to  $\gamma$  (220) at  $128^{\circ}$  and  $\alpha'$  (111) at approximately  $154^{\circ}$ – $156^{\circ}$ , and (200) at around  $105^{\circ}$ . A ferri-scope analysis estimates the martensite volume content to be approximately 41.3 %. It's important to note that the martensite volume fraction can vary depending on the measurement technique employed [36]. In the case of XRD, texture effects can influence the accuracy of the measurements [37].

Fig. 8 (a) presents the XRD analysis of AISI 420 HSMSS quenched and tempered and reveals a microstructure characterized predominantly by martensitic ( $\alpha'$ ) phase. Furthermore, the carbon content in AISI 420 SS contributes to the incomplete dissolution of (Fe,Cr)23C6 carbides during the austenitization process [23].

The sharp and well-defined peaks in the XRD pattern suggest a well-ordered crystalline structure, typical of SS subjected to high-temperature treatments, enhancing phase homogeneity and crystalline stability. In order to determine if the EDM machine has led to any residual stress on the edge of the specimens, the residual stress analysis in the deformed AISI 301LN SS (54 %) and heat treated AISI 420 are presented in Fig. 9 (a), (b), (c), (d) and uses the relationship between interplanar spacing (d-spacing) and the lattice parameter. This technique is known as the  $\sin^2\psi$  method for determining residual stresses using XRD [38]. The analyses were performed on the surface and lateral of the materials to allow comparison between the two scenarios.

It is worth mentioning that the presence of compressive residual stress on the material surface can be beneficial for fatigue resistance [38]. In contrast, annealing reduces the dislocation density and relaxes the residual stresses, leading to a significantly lower compressive residual stress in the annealed material [39]. The volume fractions of the observed  $\alpha'$ -martensite as determined by EBSD and ferri-scope, are

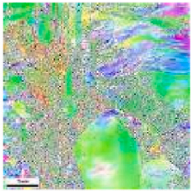
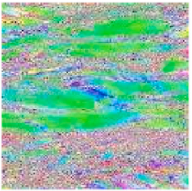

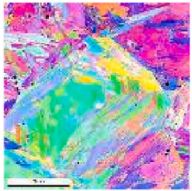
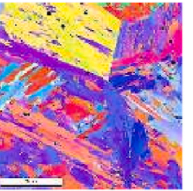
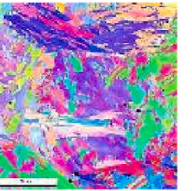
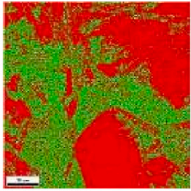
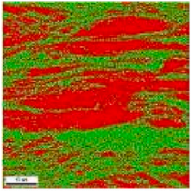
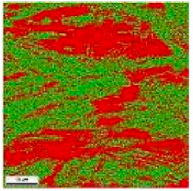
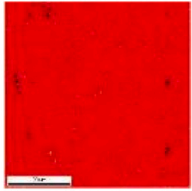
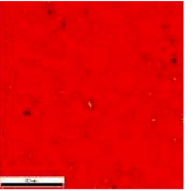
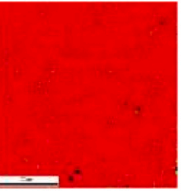
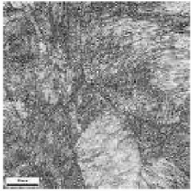
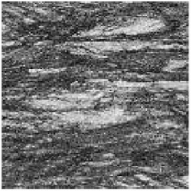
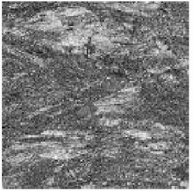
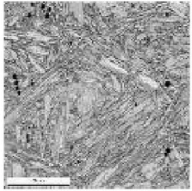
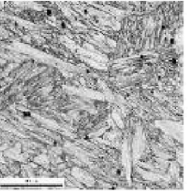
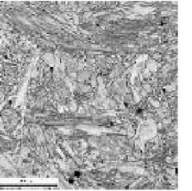
|           | AISI 301LN CR (54% plastic deformation)   |   |   | AISI 420 QT  |   |   |
|-----------|---|---|---|--|---|---|
| IPF Map   |  |  |  |  |  |  |
|           | Surface   | Longitudinal  | Transversal   | Surface  | Longitudinal  | Transversal   |
| Phase Map |  |  |  |  |  |  |
|           | <div><div>Austenite(ma)</div><div>0.6710.671</div><div>0.3290.329</div></div>     | <div><div>Austenite(ma)</div><div>0.6180.618</div><div>0.3820.382</div></div>     | <div><div>Austenite(ma)</div><div>0.5970.597</div><div>0.4030.403</div></div>     | <div><div>α-Martensite</div><div>0.9810.981</div><div>0.0190.019</div></div>       | <div><div>α-Martensite</div><div>0.9820.982</div><div>0.0180.018</div></div>        | <div><div>α-Martensite</div><div>0.9770.977</div><div>0.0230.023</div></div>        |
| IQ Map    |  |  |  |  |  |  |
|           |   |   |   |  |   |   |

Fig. 18. Comparison between IPF map, Phase map and IQ map.

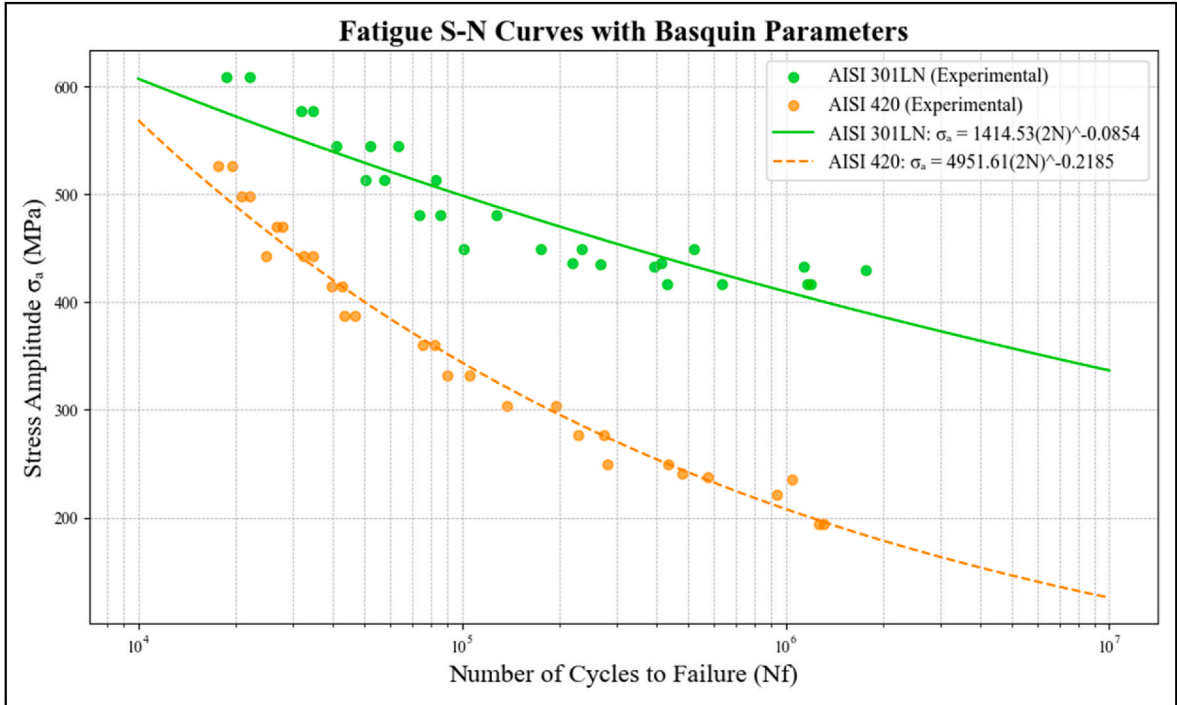


Fig. 19. The S–N curve of the HSMSS as-polished condition, AISI 301LN and AISI 420.

listed in Table 5.

The AISI 301 LN CR material, measured in the lateral-thickness longitudinal direction, exhibited significantly higher compressive residual stress ( $-321 \pm 39.3$  MPa) compared to AISI 420 QT ( $-203.5 \pm 11.2$  MPa), suggesting that the process of polishing the specimens could have played a role in increasing the compressive stress. On the material surface, AISI 301 LN CR also demonstrated notable compressive residual stress ( $-149.5 \pm 35.3$  MPa), while AISI 420 QT presented tensile

**Table 6**

HCF performance as a function of stress amplitude in as-polished samples; R = 0.1, 21Hz, room temperature 23 °C. Invalid (cracked outside working area), Run out.

| AISI 301LN  |                  |         | AISI 420   |                  |         |
|-------------|------------------|---------|------------|------------------|---------|
| Sample      | $\sigma_a$ (MPa) | Nf      | Sample     | $\sigma_a$ (MPa) | Nf      |
| #01. P301LN | 609.2            | 22033   | #01-P420D  | 526              | 17597   |
| #02. P301LN | 609.2            | 18684   | #02-P420D  | 526              | 19554   |
| #07. P301LN | 577.1            | 31933   | #03 -P420D | 498              | 22007   |
| #08. P301LN | 577.1            | 34716   | #04-P420D  | 498              | 20763   |
| #13. P301LN | 545              | 40899   | #05 -P420D | 470              | 26781   |
| #14. P301LN | 545              | 63500   | #06-P420D  | 470              | 27926   |
| #15. P301LN | 545              | 51968   | #07-P420D  | 443              | 24913   |
| #19. P301LN | 513              | 50513   | #08-P420D  | 443              | 34738   |
| #20. P301LN | 513              | 82943   | #09-P420D  | 443              | 32431   |
| #21. P301LN | 513              | 57539   | #10-P420D  | 415              | 42732   |
| #25. P301LN | 481              | 85935   | #11-P420D  | 415              | 39587   |
| #26. P301LN | 481              | 127999  | #12-P420D  | 387              | 46856   |
| #27. P301LN | 481              | 74028   | #13-P420D  | 387              | 43287   |
| #31. P301LN | 449              | 233490  | #14-P420D  | 360              | 82296   |
| #32. P301LN | 449              | 101065  | #15 -P420D | 360              | 75624   |
| #33. P301LN | 449              | 521597  | #16-P420D  | 332              | 90404   |
| #34. P301LN | 449              | 175708  | #17-P420D  | 332              | 105174  |
| #45. P301LN | 436              | 412473  | #18-P420D  | 304              | 137961  |
| #43. P301LN | 436              | 218997  | #19-P420D  | 304              | 194923  |
| #49. P301LN | 435              | 268641  | #20-P420D  | 277              | 273424  |
| #48. P301LN | 433              | 1136568 | #21-P420D  | 277              | 228722  |
| #47. P301LN | 433              | 391096  | #22-P420D  | 249              | 280938  |
| #44. P301LN | 430              | 1765166 | #23 -P420D | 249              | 434518  |
| #37. P301LN | 417              | 1198471 | #26-P420D  | 241              | 478234  |
| #38. P301LN | 417              | 637211  | #28-P420D  | 238              | 575719  |
| #39. P301LN | 417              | 428191  | #25 -P420D | 235              | 1048694 |
| #40. P301LN | 417              | 1168270 | #24-P420D  | 221              | 938743  |
|             |                  |         | #27-P420D  | 194              | 1264084 |
|             |                  |         | #29-P420D  | 194              | 1305822 |

residual stress ( $249.2 \pm 4.8$  MPa). This pronounced difference is attributed to the higher dislocation density introduced during the 54 % plastic deformation process, generating localized stress fields. These dislocations, acting as internal barriers to further plastic deformation, not only increase the compressive residual stress but also can enhance fatigue resistance by impeding crack initiation and propagation, thereby improving the material's overall durability under cyclic loading conditions [40].

### 3.3. Microstructure after martensite transformation condition

The images reveal the internal structure of the AISI 301LN SS, particularly the presence of  $\alpha'$ -martensite that appears as short, dark needles, while the untransformed  $\gamma$ R phase remains light [33,41,42]. The etching solution (Behara 10 %) has been used. The same sample (Fig. 10) was etched with a sodium hydroxide (NaOH 10 %) solution to verify the existence of any remaining secondary phases, such as  $\delta$ -Fe (delta ferrite), which was confirmed as shown Fig. 11.

Fig. 12 presents the Inverse Pole Figure (IPF) grain orientation (GO) maps for the deformed AISI 301LN ASS specimens at the surface, transverse, and middle sections of the sample, which was cut and reconstructed in a cubic format. To confirm the presence of secondary phases, specifically  $\alpha'$ -martensite, a phase map was generated, Fig. 13, providing a visual representation of the phases within the material sample, based on the crystal orientation data obtained using the EBSD technique.

To further investigate the phase transformation induced by cold work in AISI 301LN ASS, samples with a 54 % thickness reduction were analyzed using EBSD. This deformation level was chosen due to the significant strain-induced martensitic transformation observed at high deformation rates and the corresponding increase in hardness (HRC). Phase maps were utilized to determine the distribution and percentage of each phase. As show in Fig. 12, the martensite ( $\alpha'$ ) in the 54 %-reduced samples is primarily composed of ultrafine block structures.

The martensite content was approximately 38 % in the longitudinal direction and 40 % in the transverse direction. These EBSD maps qualitatively confirm that cold work significantly promotes martensitic transformation in AISI 301LN ASS [43,44].

Fig. 12 also illustrates the overall microstructure of the plastically deformed steel, which shows a heterogeneous distribution of large austenite grains and ultrafine  $\alpha'$ -martensite. The large austenite grains exhibit a strong texture along the {101} direction. The orientation spread observed in these grains (Fig. 12, X, Y, Z) indicates that they remain in a deformed state after cold working, as no annealing was performed following deformation. The texture and orientation spread along the {101} direction, are directly linked to the cold rolling process.

As previously reported by Roa et al. [45], highly deformed austenitic grains can be challenging to index accurately using the EBSD technique. In addition to previous works [7,46], untransformed austenite is the majority phase in the cold-worked material, occupying approximately 61.8 % of the area in the longitudinal direction Fig. 13 (a), and 59.7 % in the transverse direction.

Fig. 13 (b) Alpha prime ( $\alpha'$ ) martensite is also present in the longitudinal analyses, accounting for 38.2 %, and in the transverse analyses, 40.3 %, results via EBSD.

After a soaking period of 15 min at 1100 °C, the quenching process was carried out with forced air cooling and the tempering was carried out at a temperature of 250 °C, with a soaking time of 120 min, followed by air cooling. The chosen tempering temperature and soaking time were based on the work of A. N. Moura et al. [36]. For the tempering process, a resistive muffle-type electric furnace from EDG was used, with a maximum operating temperature of 1200 °C without a controlled atmosphere, where the samples were placed separately from each other on a tray.

As reported by Refs. [7,47], quenching the AISI 420 SS results in the formation of martensite containing dispersed chromium-rich (Cr,Fe) 23C6 carbides. The microstructure of the tested steel, as shown in Figs. 14 and 15, consists of martensite, retained austenite, and (Cr,Fe) 23C6 carbides.

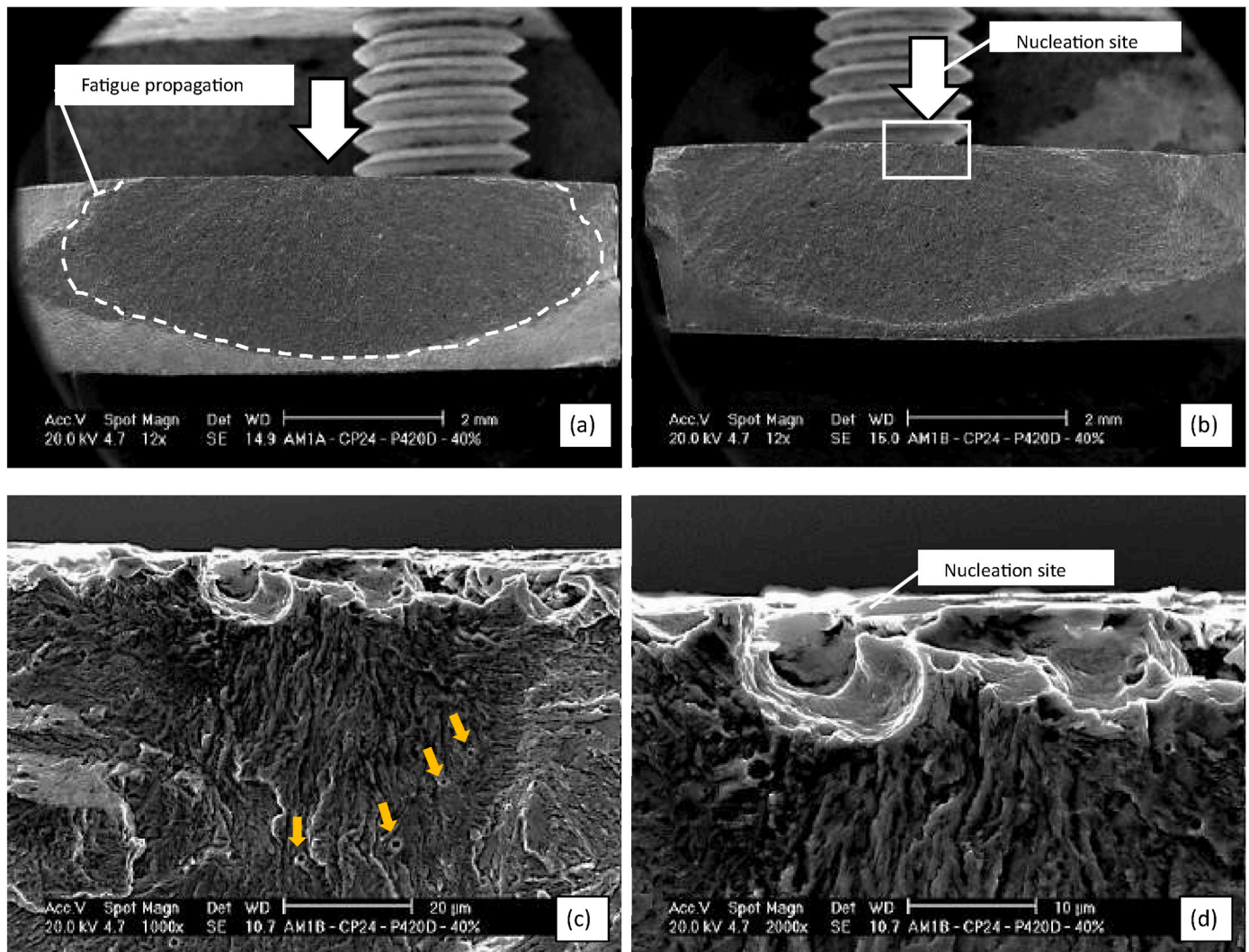
In Fig. 16 is displayed the Inverse Pole Figure (IPF) grain orientation (GO) maps for the heat-treated AISI 420 MSS specimens. The maps represent grain orientations at the surface, transversal, and longitudinal sections, which were cut and reconstructed in a cubic format as well. These orientations are color-coded based on their alignment along the {001}, {101}, and {111} planes, providing a visual representation of the texture developed during the quenching and tempering processes.

To confirm the existence of secondary phases, particularly retained austenite,  $\gamma$ R an additional phase map was generated using EBSD analysis. Fig. 17 shows the detailed views and (110) pole figures of the retained austenite in the AISI 420 HSMSS. The results indicate that the retained austenite is located between the martensite blocks. This suggests that the martensite laths formed during martensitic transformation disrupted the austenite grain, leading to the retention of austenite between the blocks, as previously reported by Marques et al. [33].

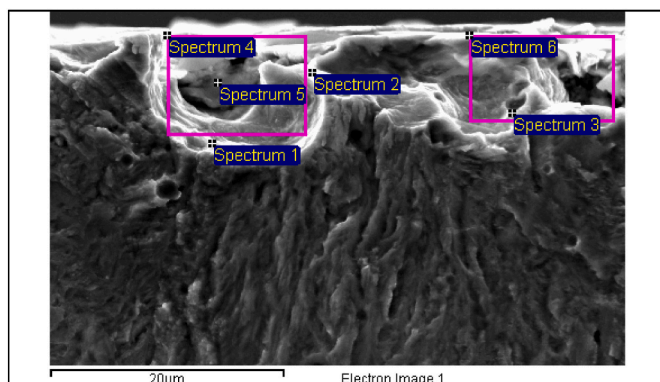
The IPF maps, along with the phase map, reveal the heterogeneous microstructure of heat-treated AISI 420 MSS, consisting of a combination of large martensite blocks, retained austenite regions, and (Cr,Fe) 23C6 carbides. The grain orientations across the normal, rolling, and transverse directions reflect the material's thermomechanical processing history, with no clear evidence of preferred grain plane orientation.

The martensite content in AISI 301LN samples rolled to 54 % reduction and AISI 420 QT samples is summarized in Fig. 18. In AISI 301LN, the average martensite volume fraction is 39.3 %, confirming that cold working promotes martensitic transformation in rolled austenitic stainless steels. The significant lattice distortion and stress concentration caused by large plastic deformation in AISI 301LN lead to substantial martensitic transformation and grain distortion. For AISI 420 QT, the martensite content is approximately 97.95 %, with a higher proportion of larger martensite blocks. This suggests that the heat treatment process used for AISI 420 effectively induced martensitic





**Fig. 20.** Fatigue fracture morphology: AISI 420 sample 24 (side I and II). (a) crack propagation perpendicular to load direction; (b) fatigue crack nucleation site; (c) spheroidal (Cr,Fe)<sub>23</sub>C<sub>6</sub> carbides; (d) magnification of the nucleation site and area chose for EDS analysis.



**Fig. 21.** EDS spectrum data of the fatigue crack initiation.

transformation, resulting in a highly martensitic microstructure [36]. Fig. 18 illustrates the IPF maps, phase maps and IQ maps across the various regions of both materials.

### 3.4. Fatigue performance

The high-strength martensitic stainless steels (HSMSS) AISI 301LN and AISI 420 were subjected to fatigue testing also at room temperature. The S–N curves for both materials, showed in Fig. 19, illustrate their performance under fatigue loading. Due to the high hardness, yield strength, and tensile strength of the martensitic structures in both alloys, relatively high-stress amplitudes were applied during testing. As expected, the fatigue life for both materials decreases as the applied stress amplitude ( $\sigma_a$ ) increases.

For AISI 301LN, at a stress amplitude of 609 MPa, a fatigue life of approximately 20,000 cycles was observed. In comparison, AISI 420 exhibited a fatigue life of around 18,500 cycles at a lower applied stress amplitude of 526 MPa. This suggests that, despite the higher stress amplitude applied to AISI 301LN, it demonstrates superior fatigue resistance relative to AISI 420. The fatigue performance of all tested HSMSS samples is presented in Table 6 and graphically represented in the  $\sigma_a - N_f$  curve (Fig. 19).

The data confirms a general trend: as the stress amplitude ( $\sigma_a$ ) increases, the number of cycles to failure ( $N_f$ ) decreases across both materials, regardless of surface finish. A comparison of the two materials reveals that AISI 301LN consistently withstands higher stress amplitudes compared to AISI 420.

A particularly prominent comparison can be made between AISI

**Table 7**

EDS Processing option: All elements analyzed (wt. - %).

| Spectrum   | C     | O     | Al   | Si   | Cl   | Ca   | Cr    | Fe    |
|------------|-------|-------|------|------|------|------|-------|-------|
| Spectrum 1 | 15.50 | –     | –    | 0.80 | –    | –    | 12.25 | 71.44 |
| Spectrum 2 | 17.25 | 0.18  | –    | 0.56 | –    | –    | 10.09 | 72.10 |
| Spectrum 3 | 11.08 | –     | –    | 0.60 | –    | –    | 12.42 | 75.90 |
| Spectrum 4 | 28.44 | 5.62  | –    | 0.71 | –    | 0.46 | 8.77  | 56.00 |
| Spectrum 5 | 52.03 | 14.78 | 0.60 | 0.69 | 0.35 | 1.38 | 4.29  | 25.88 |
| Spectrum 6 | 18.01 | –     | –    | 0.44 | –    | –    | 11.32 | 70.24 |
| Max        | 52.03 | 14.78 | 0.60 | 0.80 | 0.35 | 1.38 | 12.42 | 75.90 |
| Min        | 11.08 | 5.62  | 0.60 | 0.44 | 0.35 | 0.46 | 4.29  | 25.88 |

301LN (sample #40) and AISI 420 (sample #10) under identical test conditions ( $\sigma_a = 416$  MPa), the AISI 301LN sample exhibited nearly 27 times the fatigue life of the AISI 420 sample — a significantly better performance than initially anticipated. This result highlights the superior fatigue resistance of AISI 301LN, even under demanding conditions.

### 3.4.1. Basquin parameters analysis and material fatigue behavior

The fatigue behavior of AISI 301LN and AISI 420 stainless steels can be effectively characterized and compared using their respective Basquin parameters, which describe the stress-life ( $S - N$ ) relationship through a power law equation. This analysis highlights distinct differences in their fatigue response mechanisms, offering valuable insights into their performance characteristics and potential applications, expressed in equation (1) [48,49].

$$\sigma_a = \sigma_f' (2Nf)^b \quad (\text{Eq. 1})$$

where.

- (a)  $\sigma_a$  is the stress amplitude (MPa).
- (b)  $\sigma_f'$  is the fatigue strength coefficient (MPa).
- (c)  $Nf$  is the number of cycles to failure.
- (d)  $b$  is the fatigue strength exponent.
- (e)  $2Nf$  represents the number of reversals to failure.

The determination of the Basquin parameters was carried out by applying a logarithmic transformation to the Basquin equation (2), which is expressed as:

$$\log(\sigma_a) = \log(\sigma_f') + b \cdot \log(2Nf) \quad (\text{Eq. 2})$$

The fatigue strength exponent ( $b$ ) shows a marked difference between the two materials. AISI 301LN exhibits a  $b$  value of  $-0.0854$ , while AISI 420 shows a more negative value of  $-0.2185$ . This significant difference in slope coefficients indicates fundamentally different fatigue response mechanisms. AISI 301LN's less negative  $b$  value suggests a greater resistance to cyclic degradation, more stable microstructural response to cyclic loading, superior high-cycle fatigue performance and potentially beneficial strain-induced transformation mechanisms. AISI 420's more negative  $b$  value indicates more rapid degradation of fatigue strength with increasing cycles, higher sensitivity to cyclic loading, better performance in low-cycle fatigue regimes [48,49].

The fatigue strength coefficients present an interesting contrast, with AISI 420 showing a notably higher value (4951.61 MPa) compared to AISI 301LN (1414.53 MPa). This parameter, representing the theoretical stress at one reversal, provides insights into the materials' inherent strength characteristics. AISI 420's higher  $\sigma_f'$  suggests superior initial strength capacity, better performance in very low cycle applications, higher theoretical ultimate strength depending on tempering temperature. AISI 301LN's lower  $\sigma_f'$  indicates more moderate initial strength, better balance between strength and ductility, typical austenitic behavior and potential for strain hardening during cyclic loading [48, 49].

The goodness of fit, indicated by the  $R^2$  values, highlights the high reliability of the fatigue characterization for both materials. Specifically,

AISI 420 achieved an  $R^2$  value of 0.946, while AISI 301LN recorded an  $R^2$  value of 0.921. These high  $R^2$  values confirm a strong correlation with the Basquin relationship, demonstrating the model's robust predictability of fatigue behavior. This provides a solid foundation for design calculations and underscores the validity of using the Basquin equation for the studied materials [48–50].

### 3.5. Scanning electron microscopy - fractography

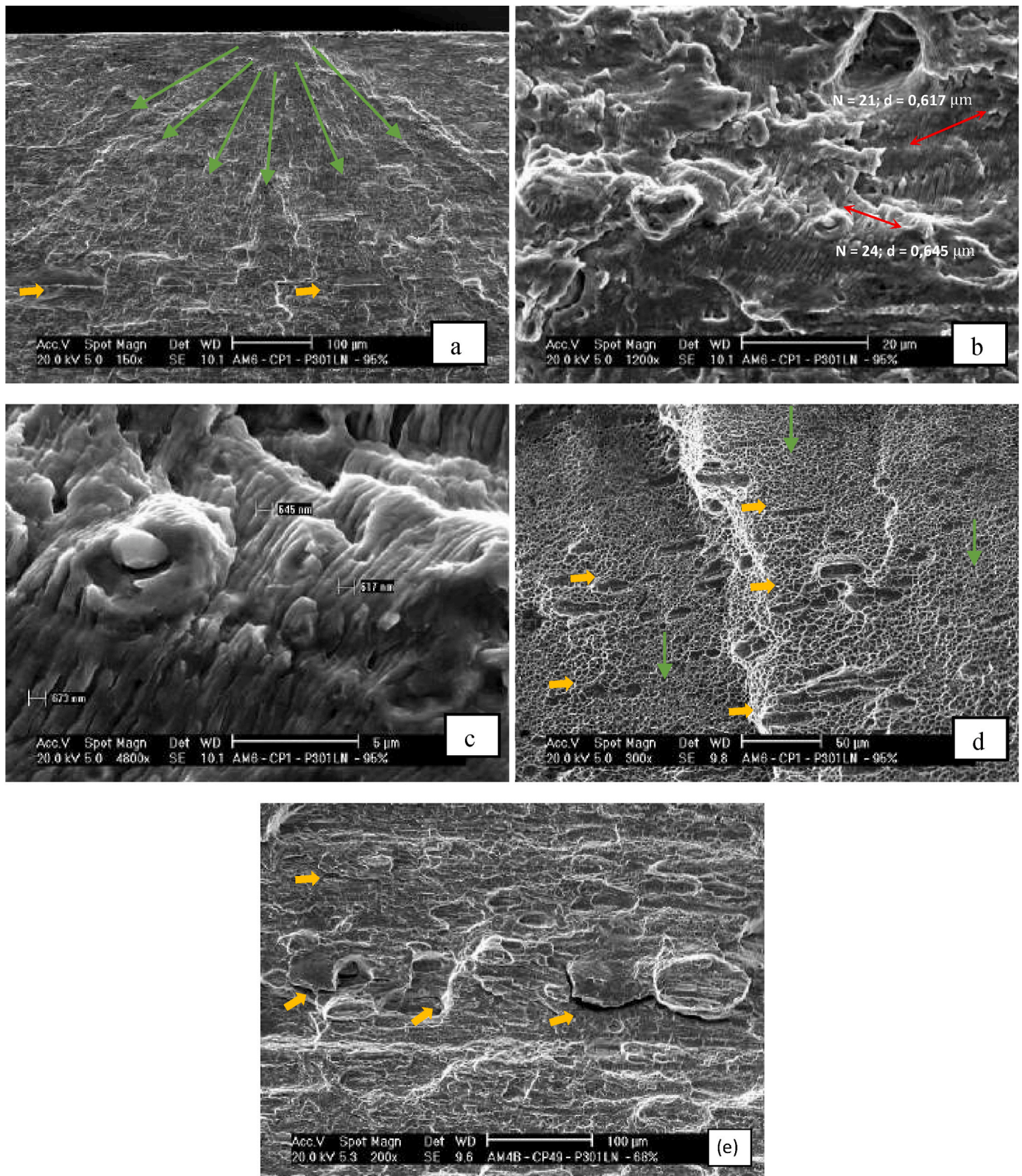
SEM images of the fractured surfaces from fatigue-tested samples are presented in Fig. 20. The selection of samples for analysis was based on those that failed before reaching their expected fatigue life based on the maximum applied stress.

The EDS spectrum data of the fatigue crack initiation site shows that there are regions with contamination or oxidation on the surface of the AISI 420 SS, Fig. 21. This is common after exposure to air or certain environments. The variation in carbon and chromium suggests the possibility of carbide formation, which is expected in AISI 420 due to its martensitic structure after heat treatment Table 7 [44].

The carbon (C) content varies considerably across the spectra, from 11.08 % to 52.03 %. These high carbon content suggests regions with presence of carbide phases (Cr,Fe)23C6, as previously suggested by A. N. Moura et al. [32], which is common in martensitic stainless steels like AISI 420 subjected to heat treatment processes [45]. Chlorine (Cl), Calcium (Ca) are present in very low amounts in specific spectra (4 and 5), possibly indicating contamination, likely from handling or environmental exposure.

In the same way as per the AISI 420 samples, SEM was utilized to investigate the fracture surfaces of fatigue-tested AISI 301LN specimens, specifically samples 1 and 49. In sample 1, a surface crack initiation site was identified Fig. 22 (a), signifying the origin of fatigue failure [46]. The fatigue crack propagation was evident, characterized by distinct striations typical of cyclic loading (b) and (c). Microcracks were observed near  $\delta$ -ferrite (d), a secondary phase present in the steel's microstructure as observed prior in the EBSD analyses. The fracture surface also displayed dimples (d), a feature indicative of ductile fracture. Sample 49: Secondary cracks oriented parallel to the applied load were detected (e). Sample #49 showed moderate surface roughness ( $R_a = 0.13 \mu\text{m}$ ,  $R_t = 1.57 \mu\text{m}$ ) and achieved a fatigue life of 268,641 cycles at 435 MPa, which falls within the expected range for this stress level. While this represents good fatigue performance, several other samples at similar or slightly lower stress amplitudes achieved longer fatigue lives - notably sample #48 (433 MPa, 1,136,568 cycles) and sample #44 (430 MPa, 1,765,166 cycles). The presence of secondary cracks oriented parallel to the applied load, as observed in fractography analysis (Fig. 20 (e)), suggests that crack propagation behavior, rather than surface roughness, was a key factor in fatigue performance. This is further supported by sample #40, which despite its smoother surface finish, achieved a significantly higher fatigue life of 1,168,270 cycles even at a lower stress amplitude of 417 MPa. These results indicate that while sample #49 demonstrated good fatigue resistance, microstructural factors and crack propagation mechanisms likely played more decisive roles than surface roughness in determining overall fatigue





**Fig. 22.** Fatigue fracture morphology: AISI 301LN sample 1 (a, b, c, d) and 49 (e). (a) Surface microstructural nucleation site in specimen 1. Green arrows show the direction of crack propagation, yellow arrows show microcracks alongside  $\delta$ -ferrite. (b) Presence of striations on the fracture surface of sample 1, close to nucleation site. N refers to the number of striations, d is the distance between each striation recorded. (c) close-up of the striations found on the fracture surface. (d) Yellow arrows indicating  $\delta$ -ferrite alignment, green arrows showing presence of dimples. (e) secondary cracks parallel to load application indicated by yellow arrows.

performance.

The phenomenon of secondary crack formation during fatigue loading has been widely documented as a mechanism that influences crack propagation behavior. Secondary cracks, particularly in materials with a higher martensite content, can alter stress distribution near the crack tip, thereby delaying the progression of the primary crack. These secondary cracks, often branching perpendicular to the crack growth direction, effectively dissipate energy and increase resistance to fatigue failure [51,52]. However, in the case of Sample 49, the detection of secondary cracks aligned parallel to the applied load suggests a distinct mechanism.

Parallel secondary cracks may act as stress redistributors, mitigating the stress intensity factor at the primary crack tip by absorbing part of the cyclic loading. This alignment could result in a shielding effect, where the stress concentration in the region is reduced, slowing the rate of fatigue crack propagation [53]. Such behavior is particularly relevant in materials with complex microstructures, where deformation-induced martensite and residual stress from cold work can influence crack initiation and propagation pathways. The formation of these parallel cracks highlights the intricate interplay between microstructure, load orientation, and crack growth mechanisms, underscoring their importance in enhancing fatigue resistance under cyclic loading conditions [54,55].

#### 4. Conclusion

The primary objective of this research was to evaluate the Green Manufacturing Impact on Fatigue Strength of AISI 301LN and AISI 420 HSMSS samples, and to identify any correlation between fatigue life, surface parameters, manufacturing processes, microstructure, and fractographic analysis. From this work, the following conclusions can be drawn.

- AISI 301LN exhibited superior fatigue resistance across all tested cycle ranges compared to AISI 420, despite their similarity in mechanical properties ( $\sigma_{UTS}$  of  $1539 \text{ MPa} \pm 2.45$  for AISI 301LN and  $1518 \text{ MPa} \pm 5.05$  for AISI 420), hardness ( $\sim 46 \text{ HRC}$ ), and roughness. This superiority is reflected in the higher fatigue strength coefficient ( $\sigma_f' = 1414.53 \text{ MPa}$ ) and a less negative Basquin slope ( $b = -0.0854$ ), indicating better resistance to fatigue, particularly at high stress amplitudes. The enhanced fatigue performance of AISI 301LN is attributed to its unique microstructure, consisting of ultrafine martensite and retained austenite, which likely improves its ability to resist crack initiation and propagation under cyclic loading conditions.
- The Basquin model provided a strong fit for both materials, with high  $R^2$  values (0.9210 for AISI 301LN and 0.9460 for AISI 420). These values demonstrate the reliability of the model for predicting fatigue behavior and its suitability for new design and engineering applications.
- AISI 420 demonstrated a steeper Basquin slope ( $b = -0.2185$ ), suggesting a faster decrease in stress amplitude capacity with increasing cycles. While its overall fatigue strength was lower, its behavior was consistent and predictable, making it suitable for applications requiring moderate fatigue resistance.
- The transformation-induced martensite in AISI 301LN, combined with retained austenite, produced a very refined microstructure that offers a more resistant crack propagation path. In contrast, AISI 420, with its heat-treated martensitic structure, exhibited a coarser microstructure than AISI 301LN. The higher C content in AISI 420 led to the formation of carbide phases ((Cr,Fe)23C6) during heat treatment, which became the preferred sites for crack initiation. Additionally, surface contamination and oxidation observed on AISI 420 samples contributed to its inferior fatigue performance.

• Residual compressive stress also played a significant role in enhancing fatigue resistance in the presence of fine surface defects such as  $\delta$ -ferrite. These stresses acted to retard crack propagation, leading to improved fatigue life in AISI 301LN.

- Both AISI 301LN and AISI 420 stainless steels were produced through a green manufacturing process certified by ResponsibleSteel™, emphasizing sustainability and reduced carbon emissions. The superior fatigue performance of AISI 301LN, combined with its environmentally responsible production, highlights the potential for advanced materials that balance high performance with sustainability. The findings reinforce the importance of sustainable practices in developing high-strength steels that meet demanding engineering requirements while aligning with global efforts to reduce environmental impact. This approach ensures that innovative materials like AISI 301LN can contribute to greener and more sustainable applications in industries such as aerospace, automotive, and structural engineering.

The authors declare that they have no known competing financial interests or personal relationships that could have appeared to influence the work reported in this paper.

#### CRedit authorship contribution statement

**Maurício Pinheiro dos Santos:** Writing – review & editing, Writing – original draft, Software, Methodology, Investigation, Conceptualization. **Elaine Carballo Siqueira Corrêa:** Writing – review & editing, Validation, Supervision, Methodology, Investigation, Conceptualization. **Geovane Martins Castro:** Writing – review & editing, Supervision, Methodology, Investigation, Conceptualization. **Waldek Wladimir Bose Filho:** Writing – review & editing, Validation, Supervision, Methodology. **Rodrigo Magnabosco:** Writing – review & editing, Validation, Supervision, Methodology. **Wellington Lopes:** Writing – review & editing, Validation, Supervision, Methodology. **Wilian da Silva Labiapari:** Writing – review & editing, Validation, Supervision, Methodology.

#### Data availability

The raw/processed data required to reproduce these findings cannot be shared at this time due to legal or ethical reasons.

#### Declaration of competing interest

The authors declare that they have no known competing financial interests or personal relationships that could have appeared to influence the work reported in this paper.

#### Acknowledgments

The authors would like to thank the Aperam South America Research Center for their generous support, including providing the resources for analysis and donating materials.

#### References

- [1] Lee Y-S, Kondo Y, Okayasu M. Friction-induced martensitic transformation and wear properties of stainless steel under dry and wet conditions. *Metals* Jun. 2020; 10(6):743. <https://doi.org/10.3390/met10060743>.
- [2] Aslam R, Mobin M, Zehra S, Aslam J. A comprehensive review of corrosion inhibitors employed to mitigate stainless steel corrosion in different environments. *J Mol Liq* Oct. 2022;364:119992. <https://doi.org/10.1016/j.molliq.2022.119992>.
- [3] Bergengren Y, Larsson M, Melander A. Fatigue properties of stainless sheet steels in air at room temperature. *Mater Sci Technol* Dec. 1995;11(12):1275–80. <https://doi.org/10.1179/mst.1995.11.12.1275>.
- [4] Singh R. “Applied welding engineering: processes, codes, and standards, third edition,”. *Applied welding engineering: processes, codes, and standards*. Jan. 2020. p. 1–420. <https://doi.org/10.1016/C2019-0-03490-5>. Third Edition.
- [5] Chiaverini V. *Tratamentos Térmicos das Ligas Metálicas*. 2003. p. 263.



- [6] Callister's materials science and engineering - google books [Online]. Available, [https://www.google.com/books/edition/Callister\\_s\\_Materials\\_Science\\_and\\_Engine/IUjODwAAQBAJ?hl=en&gbpv=1&printsec=frontcover](https://www.google.com/books/edition/Callister_s_Materials_Science_and_Engine/IUjODwAAQBAJ?hl=en&gbpv=1&printsec=frontcover). [Accessed 1 January 2025].
- [7] Krauss G. *Steels: processing, structure, and performance*. first ed. Materials Park, Ohio: ASM; 2005.
- [8] De Alcântara CM, et al. Microstructure and pitting corrosion resistance of quenched, single tempered and double tempered AISI 420 martensitic stainless steel. *Mater Res Oct*. 2021;24(6):e20210093. <https://doi.org/10.1590/1980-5373-MR-2021-0093>.
- [9] "Economic outlook for Southeast Asia, China and India 2024,". May 2024. <https://doi.org/10.1787/3BBE7DFE-EN>.
- [10] Ossa EA, Paniagua M. Handbook of materials failure analysis with case studies from the aerospace and automotive industries. *Handbook Mater Failure Anal Case Stud Aero Automot Ind* 2016:167–90 [Online]. Available: <http://www.scopus.com/inward/record.url?eid=2-s2.0-84943155386&partnerID=tZOTx3y1>. [Accessed 1 January 2025].
- [11] Kassouri Y, Alola AA, Savaş S. The dynamics of material consumption in phases of the economic cycle for selected emerging countries. *Resour Policy Mar*. 2021;70:101918. <https://doi.org/10.1016/J.RESOURPOL.2020.101918>.
- [12] Reed-Hill RE, Abbaschian R, Abbaschian L. *Physical metallurgy principles*. fourth ed. Stamford: Cengage Learning; 2009.
- [13] Madoo A. Generalized continuum mechanics and engineering applications. Generalized continuum mechanics and engineering applications. Oct. 2015. p. 1–136. <https://doi.org/10.1016/C2014-0-04708-9>.
- [14] South America A. STAINLESS STEEL technical specifications. [www.aperam.com](http://www.aperam.com). [Accessed 1 January 2025].
- [15] Stainless steel price - what's the price of stainless steel?. <https://www.ryerson.com/metal-resources/metal-market-intelligence/what-is-the-current-price-of-stainless-steel>. [Accessed 4 January 2025].
- [16] MEPS global steel prices & indices | historical steel prices. <https://mepsinternational.com/gb/en/prices-and-indices>. [Accessed 4 January 2025].
- [17] "Guide for preparation of metallographic specimens,". Jun. 2017. <https://doi.org/10.1520/E0003-11R17>.
- [18] "Test methods for determination of carbon, sulfur, nitrogen, and oxygen in steel, iron, nickel, and cobalt alloys by various combustion and fusion techniques,". Mar. 2011. <https://doi.org/10.1520/E1019-11>.
- [19] ASTM. ASTM E8/E8M standard test methods for tension testing of metallic materials 1. Annu Book ASTM (Am Soc Test Mater) Stand 2010;4(C):1–27. <https://doi.org/10.1520/E0008>.
- [20] "Test methods for vickers hardness and knoop hardness of metallic materials,". Apr. 2017. <https://doi.org/10.1520/E0092-17>.
- [21] "Practice for conducting force controlled constant amplitude axial fatigue tests of metallic materials,". Jun. 2021. <https://doi.org/10.1520/E0466-21>.
- [22] Geometrical product specifications (GPS)-Surface texture: profile-Part 3: specification operators(E) COPYRIGHT PROTECTED DOCUMENT [Online]. Available: [www.iso.org](http://www.iso.org). [Accessed 1 January 2025].
- [23] de Moura AN, et al. Effect of austenitization temperature on microstructure, crystallographic aspects, and mechanical properties of AISI 420 martensitic stainless steel. *Mater Sci Eng, A Sep*. 2024;909:146835. <https://doi.org/10.1016/J.MSEA.2024.146835>.
- [24] "Test method for microindentation hardness of materials,". Jun. 2017. <https://doi.org/10.1520/E0384-17>.
- [25] Isfahany AN, Saghaian H, Borhani G. The effect of heat treatment on mechanical properties and corrosion behavior of AISI420 martensitic stainless steel. *J Alloys Compd Mar*. 2011;509(9):3931–6. <https://doi.org/10.1016/J.JALLCOM.2010.12.174>.
- [26] Hedström P, Lienert U, Almer J, Odén M. Stepwise transformation behavior of the strain-induced martensitic transformation in a metastable stainless steel. *Scr Mater Feb*. 2007;56(3):213–6. <https://doi.org/10.1016/j.scriptamat.2006.10.009>.
- [27] Dowling NE, Kampe SL, Kral MV. *Mechanical behavior of materials*. fifth ed. Harlow: Pearson Education Limited; 2020. p. 2019.
- [28] Ednie L, et al. The effects of surface finish on the fatigue performance of electron beam melted Ti–6Al–4V. *Mater Sci Eng, A Nov*. 2022;857:144050. <https://doi.org/10.1016/J.MSEA.2022.144050>.
- [29] Fuchs HO, Stephens RI, Saunders H. Metal fatigue in engineering (1980). *J Eng Mater Technol Oct*. 1981;103(4):346. <https://doi.org/10.1115/1.3225026>.
- [30] Grigoriev SN, Volosova MA, Okunkova AA, Fedorov SV. Influence of defects in surface layer of Al<sub>2</sub>O<sub>3</sub>/TiC and SiAlON ceramics on physical and mechanical characteristics. *Ceramics* 2023;6:818–36. <https://doi.org/10.3390/CERAMICS6020047>. vol. 6, no. 2, pp. 818–836, Mar. 2023.
- [31] Bannantine JA, Comer JJ, Handrock JL. *Fundamentals of metal fatigue analysis*, 27. New Jersey: Prentice Hall; 1990. p. 5. <https://doi.org/10.5860/choice.27-2735>.
- [32] MMPDS-04. *Metallic materials properties development and standardization (MMPDS)*. Federal Aviation Administration 2008 [Washington, D.C.].
- [33] Marques MCS, et al. Microstructure and mechanical properties of a martensitic stainless steel (0.2 %C–12 %Cr) after quenching and partitioning (Q&P) process. *J Mater Res Technol May* 2023;24:3937–55. <https://doi.org/10.1016/J.JMRT.2023.04.018>.
- [34] Talonen J, Nenonen P, Pape G, Hänninen H. Effect of strain rate on the strain-induced  $\gamma \rightarrow \alpha'$ -martensite transformation and mechanical properties of austenitic stainless steels. *Metall Mater Trans A Phys Metall Mater Sci* 2005;36 A(2):421–32. <https://doi.org/10.1007/S11661-005-0313-Y/METRICS>.
- [35] Chiaverini V. *Tratamento Térmico das Ligas Metálicas*. second ed. São Paulo: Associação Brasileira de Metalurgia e Materiais; 2008.
- [36] de Moura AN, et al. Microstructure and crystallographic texture of martensitic stainless steels after cold rolling and subsequent recrystallization. *Mater Char* 2022;192(December 2021). <https://doi.org/10.1016/j.matchar.2022.112190>.
- [37] Rivero IV, Ruud CO. Determination of the accuracy of phase analysis measurements on spherical surfaces through X-ray diffraction. *NDT E Int Sep*. 2008;41(6):434–40. <https://doi.org/10.1016/J.NDTEINT.2008.03.007>.
- [38] Delbergue D, Texier D, Bocher P, Lévesque M. Comparison of two x-ray residual stress measurement methods:  $\sin^2 \psi$  and  $\cos \alpha$ , through the determination of a martensitic steel x-ray elastic constant. *Residual Stresses* 2016;2:55–60. <https://doi.org/10.21741/9781945291173-10>. Jan. 2017.
- [39] Lin YC, Zhu JS, Chen JY, Wang JQ. Residual-stress relaxation mechanism and model description of 5052H32 Al alloy spun ellipsoidal heads during annealing treatment. *Adv Manuf Mar*. 2022;10(1):87–100. <https://doi.org/10.1007/S40436-021-00367-W/FIGURES/10>.
- [40] Oevermann T, Wegener T, Liehr A, Hübner L, Niendorf T. Evolution of residual stress, microstructure and cyclic performance of the equiatomic high-entropy alloy CoCrFeMnNi after deep rolling. *Int J Fatig Dec*. 2021;153:106513. <https://doi.org/10.1016/J.IJFATIGUE.2021.106513>.
- [41] Liu J, Deng XT, Huang L, Wang ZD. High-cycle fatigue behavior of 18Cr-8Ni austenitic stainless steels with grains ranging from nano/ultrafine-size to coarse. *Mater Sci Eng, A Aug*. 2018;733:128–36. <https://doi.org/10.1016/J.MSEA.2018.07.043>.
- [42] Huang L, et al. Mechanical origin of martensite-like structures in two-dimensional ReS<sub>2</sub>. *Commun Mater* 2021;2(1):1–10. <https://doi.org/10.1038/s43246-021-00190-7>. Aug. 2021.
- [43] Cui C, Gu K, Weng Z, Zhang M, Wang J. Martensitic transformation in rolled 301 stainless steel induced by cryogenic treatment. *Mater Today Commun Mar*. 2024;38:108531. <https://doi.org/10.1016/J.JMTCOMM.2024.108531>.
- [44] He BB, Pan S. Revealing the intrinsic nanohardness of retained austenite grain in a medium Mn steel with heterogeneous structure. *Mater Char Jan*. 2021;171:110745. <https://doi.org/10.1016/J.MATCHAR.2020.110745>.
- [45] Roa JJ, Fargas G, Calvo J, Jiménez-Piqué E, Mateo A. Plastic deformation and damage induced by fatigue in TWIP steels. *Mater Sci Eng, A Mar*. 2015;628:410–8. <https://doi.org/10.1016/J.MSEA.2015.01.043>.
- [46] Bhadeshia HKDH, Honeycombe SR. Steels: microstructure and properties. *Steels: microstructure and properties*. Jan. 2006. p. 1–344. <https://doi.org/10.1016/B978-0-7506-8084-4.X5000-6>.
- [47] Leso TP, Mukarati TW, Mostert RJ, Siyasiya CW. Strain-induced martensitic transformation and the mechanism of wear and rolling contact fatigue of AISI 301LN metastable austenitic stainless steel. *Steel Res Int Sep*. 2024;95(9). <https://doi.org/10.1002/SRIN.202400128>.
- [48] Kun F, Carmona HA, Andrade JS, Herrmann HJ. Universality behind Basquin's law of fatigue. *Phys Rev Lett Mar*. 2008;100(9). <https://doi.org/10.1103/PHYSREVLETT.100.094301/FIGURES/4/THUMBNAI>.
- [49] Strzelecki P. Determination of fatigue life for low probability of failure for different stress levels using 3-parameter Weibull distribution. *Int J Fatig Apr*. 2021;145:106080. <https://doi.org/10.1016/J.IJFATIGUE.2020.106080>.
- [50] Özdeş H, Tiryakioglu M. On estimating high-cycle fatigue life of cast Al-Si-Mg-(Cu) alloys from tensile test results. *Mater Sci Eng, A Mar*. 2017;688:9–15. <https://doi.org/10.1016/J.MSEA.2017.01.106>.
- [51] Huang M, Yuan J, Wang J, Wang L, Mogucheva A, Xu W. Role of martensitic transformation sequences on deformation-induced martensitic transformation at high strain rates: a quasi in-situ study. *Mater Sci Eng, A Jan*. 2022;831:142319. <https://doi.org/10.1016/J.MSEA.2021.142319>.
- [52] Quan H, Alderliesten RC. The energy dissipation during fatigue crack growth in metallic materials. *Eng Fract Mech Jun*. 2022;269:108567. <https://doi.org/10.1016/J.ENGFRACMECH.2022.108567>.
- [53] Hutchinson JW. Crack tip shielding by micro-cracking in brittle solids. *Acta Metall Jul*. 1987;35(7):1605–19. [https://doi.org/10.1016/0001-6160\(87\)90108-8](https://doi.org/10.1016/0001-6160(87)90108-8).
- [54] McBagonluri F, Soboyejo W. Mechanical properties: fatigue. *Encyclopedia of Condensed Matter Physics Jan*. 2005:291–8. <https://doi.org/10.1016/B0-12-369401-9/00573-8>.
- [55] Lu W, He C. Numerical simulation on the initiation and propagation of synchronous perforating fractures in horizontal well clusters. *Eng Fract Mech May* 2022;266:108412. <https://doi.org/10.1016/J.ENGFRACMECH.2022.108412>.